Carbon 260 (2026) 121941

Contents lists available at ScienceDirect

Carbon

journal homepage: www.elsevier.com/locate/carbon

Water as a decisive factor in the thermal transformation of cellulose into activated carbon

Alexa Scheer [a], Hoang Bao Tran Nguyen [c,d], Johanna Fischer [c], Glen J. Smales [b], Julian Selinger [a,f], Ahmad Alem [e], Christine Bandl [e], Steffen Fischer [c], Daria Mikhailova [d], Stefan Spirk [a,*]

[a] Institute of Bioproducts and Paper Technology, Graz University of Technology, Inffeldgasse 23, Graz, 8010, Austria
[b] Institute of Inorganic Chemistry, Graz University of Technology, Stremayrgasse 9/IV, Graz, 8010, Austria
[c] Institute of Plant and Wood Chemistry, Dresden University of Technology, Pienner Str. 19, Tharandt, 01737, Germany
[d] Karlsruhe Institute of Technology (KIT), Institute for Applied Materials (IAM), Hermann-von-Helmholtz-Platz 1, Eggenstein-Leopoldshafen, 76344, Germany
[e] Institute of Chemistry of Polymeric Materials, Technical University of Leoben, Otto Glöckel-Strasse 2, Leoben, A-8700, Austria
[f] Department of Bioproducts and Biosystems, Aalto University, P.O. Box 16300, Aalto, 00076, Finland

ARTICLE INFO

Keywords:
Activated carbon
Cellulose
One-step KOH activation
KOH solution impregnation
Water volume
Pore structure control

ABSTRACT

One-step KOH activation enables the direct conversion of cellulose-based biomass into activated carbon (AC), yet reproducible control over pore structure and carbon yield remains challenging. While many studies emphasize the KOH-to-precursor mass ratio, the water volume used for dissolving a fixed amount of KOH is rarely regarded as an independent parameter. Here, we demonstrate that the amount of water introduced with the KOH solution and its spatial distribution within the cellulose precursor after impregnation, either absorbed into the internal fiber network or retained as excess liquid, govern the thermal transformation pathway and the resulting AC properties. Using paper sheets with a defined absorption capacity as a model precursor, ACs were prepared at constant KOH loading (1:1) while systematically varying the added water volume. This approach establishes distinct initial conditions, ranging from complete solution uptake to excess external solution. Combined thermal analysis (TGA-MS), ATR-FTIR, XRD, XPS, electron microscopy, N_2 adsorption, and SAXS reveal that exceeding the precursor's absorption capacity promotes early carbonate formation, enhances alkaline degradation, delays char formation, reduces carbon yield from ~9% for C35 to ~1% for C20, and strengthens CO_2-assisted physical activation, leading to larger pores. In contrast, reduced water addition shifts the pathway toward earlier charring, limits the conversion of hydroxide into carbonate, increases yield, and promotes micropore-dominated structures. These findings identify water volume at constant KOH loading as a decisive variable in the investigated solution-impregnation system and demonstrate that it should be controlled alongside the activator-to-precursor mass ratio when targeting reproducible AC properties.

1. Introduction

Activated carbon (AC) is a porous, electrically conductive carbon material and its application-relevant properties are largely governed by pore architecture and surface chemistry [1–3]. Due to its high internal surface area, tunable porosity, and chemical stability, AC has been extensively studied for electrochemical energy storage (e.g., supercapacitors and battery electrodes) [4,5], gas adsorption/storage (e.g., CO_2 capture, H_2 storage) [2,6,7] and water treatment (removal of dyes, pharmaceuticals, and heavy metals) [3,8]. For supercapacitors, pore size distribution (PSD) must balance charge storage and ion transport. Ultramicropores (≤0.7 nm) and micropores (≤2 nm) provide most of the surface area for charge storage. However, purely microporous networks often suffer from transport limitations at high charge rates. Introducing mesopores (2-50 nm) and macropores (>50 nm) can reduce diffusion limitations and electrolyte resistance [9,10]. Consequently, the ability to engineer a targeted hierarchy of micro-/mesoporosity is central to AC design for fast-charging devices. For gas storage and separation, the "optimal" porosity shifts toward smaller pores. In physisorption-based hydrogen storage, ultramicropores dominate uptake at low pressure

* Corresponding author.
E-mail address: stefan.spirk@tugraz.at (S. Spirk).

https://doi.org/10.1016/j.carbon.2026.121941
Received 13 March 2026; Received in revised form 16 July 2026; Accepted 28 July 2026
Available online 29 July 2026

[11,12]. These examples demonstrate that high surface area alone is not a sufficient design criterion, rather, AC synthesis must be controllable enough to deliver application-specific PSDs.

Activation methods are typically classified as physical (e.g. CO_2 and/or steam gasification) [13], chemical (impregnation with activating agents such as KOH, K_2CO_3, NaOH, or phosphoric acid followed by heat treatment) [1,14–18], or a combination of both [19]. Among chemical activators, KOH is widely used because it can generate high specific surface areas (SSAs) ranging from 1000 to 4000 m^2/g and large micropore volumes [1,14,15]. KOH activation is described by a combination of (i) redox etching of carbon, (ii) gasification reactions involving $H_2O/CO/CO_2/H_2$, and (iii) intercalation of elemental potassium into carbon lattices, which expands carbon layers and contributes to micropore formation upon its removal [14,20,21].

Producing AC from biomass and biowaste offers a route toward lower-cost sorbents and electrodes while supporting circular economy concepts. Numerous precursors, including organic waste materials such as nut shells, sawdust, spent coffee grounds or brewer's spent grain have been converted into ACs for water purification and energy-related applications [2,22,23]. However, biomass-derived ACs often exhibit batch-to-batch variability [24]. In real feedstocks, precursor properties can shift with harvesting season, storage history, and processing, which complicates the reproducible production of a defined pore structure [25–27]. The precursor microstructure governs the interaction with chemical activators such as KOH and, consequently, the PSD and SSA of the AC. Limited accessibility in more crystalline or dense regions leads to heterogeneous absorption of the KOH solution, thereby affecting the intensity and uniformity of etching during activation [1].

In contrast to conventional two-step KOH activation, in which the biomass is first carbonized into a hydrophobic char prior to solution impregnation, direct impregnation of the biomass followed by conversion to AC in a single thermal treatment enables intimate KOH-precursor contact at the molecular scale [20,28]. This approach is particularly well suited to cellulosic precursors, as cellulose contains abundant oxygen-containing functional groups and a microfibrillar architecture that promote strong interactions with alkaline solutions and facilitate efficient uptake of KOH [20,28,29]. Numerous studies have focused on identifying activation temperature, dwell time, and the KOH to precursor mass ratio that maximize SSA without excessive burn-off [14,26,30]. Increasing these parameters generally enhances SSA and pore volume up to an optimum, beyond which over-etching can cause pore widening or structural collapse, reducing SSA and yield. Recent studies on biomass-derived carbons have continued to tailor porosity primarily through these conventional variables. For example, the KOH-to-biochar ratio and activation temperature were systematically varied for brewer's spent grain-derived carbons, with higher KOH loading promoting additional porosity and higher activation temperatures contributing to pore widening [31]. Pine-wood-derived carbons were likewise tailored by varying the KOH loading and the composition of $KOH/K_2C_2O_4$ activation mixtures [7]. A recent waste-paper study used aqueous KOH impregnation at a fixed KOH-to-paper mass ratio of 1:1, but neither the applied water volume nor the KOH solution concentration was reported [32].

Even when KOH loading and thermal conditions are kept constant, the amount of water used to dissolve KOH can create distinct precursor states before heat treatment. This parameter is particularly relevant for solution impregnation, which is widely used for biomass precursors [6,26,32,33] alongside physical mixing with solid KOH [14,15]. In solution impregnation, water serves as a transport medium for dissolved KOH and therefore directly affects its distribution within the precursor, whereas dry mixing is governed by solid-solid contact, KOH particle size, and mixing homogeneity. The present study consequently focuses specifically on solution-based impregnation. Despite its mechanistic relevance, the applied water volume is rarely reported and has not generally been isolated from changes in activator loading or other preparation variables.

Studies using other chemical activators further indicate that the impregnation medium can influence activation outcomes. In H_3PO_4 activation, varying the water-to-H_3PO_4 ratio affected phosphorus uptake, carbon yield, SSA, micropore volume, and PSD [34]. In $ZnCl_2$ activation, aqueous impregnation and dry mixing at identical activator-to-precursor ratios produced different structural and textural properties, which was attributed to improved activator penetration and distribution during solution impregnation [35]. However, the H_3PO_4 study varied water content together with activator uptake, while the $ZnCl_2$ study compared wet and dry preparation routes without varying the solvent volume. Neither study therefore isolated solvent volume as an independent parameter at constant activator mass.

At constant KOH loading, the water volume used to dissolve KOH determines whether the solution is fully absorbed by the precursor or remains as excess liquid, thereby influencing the spatial distribution and effective uptake of KOH within the matrix. Consequently, distinct initial precursor conditions are created for the early stages of pyrolysis, which can lead to different thermal conversion pathways and AC structures. Non-uniform impregnation, for example, can cause localized over-etching and pore collapse in KOH-rich regions during high-temperature treatment, while KOH-poor regions remain under-activated [1]. The water volume also influences drying kinetics and the time-temperature window in which KOH can undergo side reactions before the onset of high-temperature activation. Literature reports show that KOH can convert into less reactive potassium salts already at low temperatures during drying in air [16,36]. Even in an inert atmosphere, potassium-containing cellulose releases CO_2 during the initial stages of pyrolysis at temperatures below 300 °C [16,37–39], which can further consume hydroxide. Consequently, at fixed KOH mass, the water volume can determine how much reactive hydroxide remains available in the activation-relevant temperature range and how strongly it contributes to micropore formation.

This work examines how the solution volume, varied through the amount of water used to dissolve a constant KOH mass, affects cellulose-to-AC conversion and the resulting PSD, SSA, and yield. To isolate this variable, the activation temperature, dwell time, and KOH-to-precursor mass ratio were fixed at 750 °C, 1 h, and 1:1, respectively. The selected temperature lies within the range commonly investigated for KOH activation, while using a single defined KOH loading avoids coupling the solution-volume effect with changes in activator dosage. Paper sheets were selected because they provide a reproducible cellulose network with defined mass and structure, making them suitable for systematically varying liquid uptake under controlled conditions. Our approach exploits the finite maximum uptake volume of aqueous KOH in paper sheets of defined mass. The applied water volume therefore determines whether the solution is fully absorbed by the sheet or whether an external liquid fraction persists as film or pooled solution in the crucible. By systematically varying this parameter at constant KOH mass, the influence of liquid volume can be directly isolated, revealing how it shapes pyrolytic conversion and thereby governs porosity development and carbon yield. Elucidating this relationship enhances reproducibility, enables targeted pore structure design and provides valuable input for scaling up KOH-based biomass activation processes.

2. Materials and methods

2.1. Materials

Paper precursors were prepared from commercial unbeaten bleached hardwood pulp provided by Lenzing (Lenzing, Austria). Activation was performed using KOH solutions of varying concentrations prepared from KOH pellets (≥85%, Merck, Darmstadt, Germany), while 1 M HCl (Merck, Darmstadt, Germany) was employed for post-carbonization washing. All chemicals were used as received.

2.2. Preparation of ACs

Precursor papers with a grammage of 160 g/m^2 were produced using a Rapid-Köthen sheet former according to ISO 5269-2, cut into sheets of similar dimensions, and stored in a climate-controlled room at 23 °C and 50% relative humidity (ISO 187).

The maximum uptake volume of aqueous KOH by the paper sheets was determined in preliminary tests. In these, each sheet was weighed and a KOH solution containing a dry KOH mass equal to the sheet mass (KOH:paper = 1:1, w/w) was prepared while increasing the added water stepwise. After each step, the solution was applied and complete absorption (uniform wetting with no external liquid) was assessed visually. The highest water addition still yielding complete absorption corresponded to 35 w.% KOH. Subsequently, KOH solutions of 20, 25, 30, and 35 w.% were prepared. To maintain a constant KOH-to-paper mass ratio (1:1, w/w), the required volume for each sheet was calculated as

$$V_{KOH\ solution} = \frac{m_{sheet}}{w * \rho} \quad (1)$$

where $V_{KOH\ solution}$ is the applied solution volume, m_{sheet} is the sheet mass, w is the KOH mass fraction, and ρ is the solution density. Lower-concentration solutions therefore require larger volumes, thereby enabling systematic variation of the water content in the applied KOH solution across the sample series.

The sheets were impregnated in an Al_2O_3 crucible using a pipette and then directly transferred into a tube furnace (TZF 15/610, Carbolite, Neuhausen, Germany). In the tube furnace, specimens were dried at 120 °C for 1 h in a N_2 atmosphere (320 mL/min; heating rate 5 °C/min), then heated to 750 °C and held at this temperature for 1 h. After the thermal treatment, the ACs were washed with 1 M HCl and distilled water to neutral pH and dried at 105 °C overnight before storage in sealed containers. To assess intermediate stages of thermal conversion, an additional set of samples was removed from the furnace upon reaching 250 °C, photographed, and subsequently analyzed by XRD and FTIR.

2.3. Characterization

2.3.1. Thermogravimetric analysis (TGA) with/without coupled mass spectrometer (TGA-MS)

Thermogravimetric analysis (TGA) was carried out on a Netzsch 449-F1 Jupiter instrument (Netzsch, Selb, Germany) to study the thermal behavior of the KOH-impregnated precursors (C20–C35). 20 mg of specimen was placed in a ceramic crucible and heated from 30 to 750 °C at 5 °C min^{-1} under a constant nitrogen flow. Isothermal steps of 1 h were applied at 120 °C and 750 °C to replicate the drying and activation stages in the tube furnace. For specimens C20 and C35, additional TGA-MS measurements were performed using a PerkinElmer TGA 8000 (PerkinElmer, Connecticut, USA) thermogravimetric analyzer under nitrogen atmosphere. The temperature program was identical to that used for the TGA measurements without MS coupling. Volatile decomposition products were monitored online using a Shimadzu GCMS-QP2010 SE single quadrupole mass spectrometer (Shimadzu Europa GmbH, Duisburg, Germany) operated with electron ionization (EI) at 70 eV.

2.3.2. Attenuated total reflection fourier-transform infrared spectroscopy (ATR-FTIR)

ATR-FTIR spectra of the partially carbonized papers after 250 °C were recorded using an Agilent Cary 630 spectrometer (Santa Clara, CA, USA) fitted with a diamond ATR accessory and a spectral resolution of <2 cm^{-1}. Measurements were carried out in the range of 4000-650 cm^{-1}, with 64 scans averaged per spectrum. Data processing and analysis were performed with OriginPro 2020.

2.3.3. X-ray diffraction (XRD)

X-ray diffraction (XRD) measurements were performed using a STADI P diffractometer (STOE, Darmstadt, Germany) operated in transmission geometry. Monochromatic Mo $K\alpha_1$ radiation with a wavelength of λ = 0.70930 Å was employed as the X-ray source. The diffractograms were recorded over a 2θ range from 4° to 55°, using a step size of Δ2θ = 0.015°.

2.3.4. X-ray Photoelectron Spectroscopy (XPS)

Surface chemical analysis was performed using a Nexsa G2 X-ray Photoelectron Spectroscopy (XPS) system (Thermo Fisher Scientific, USA). X-ray source: monochromatic Al Kα radiation. Specimens were analyzed under ultra-high vacuum conditions ($\leq 1 \times 10^{-8}$ mbar). To enhance data reliability, measurements represent the average of two randomly selected spots (200 μm in diameter). Survey scans were carried out at a pass energy of 100 eV and an energy resolution of 1.0 eV, whilst high-resolution spectra were recorded at a pass energy of 20 eV and a resolution of 0.1 eV.

2.3.5. Scanning electron microscopy (SEM)

Scanning electron microscopy (SEM) of the AC specimens was performed using a TESCAN VEGA3 microscope (TESCAN, Czech Republic) equipped with a secondary electron detector. The microscope was operated at an acceleration voltage of 10 kV with a tungsten cathode as the electron source. AC specimens were examined without additional coating and mounted on the sample holder using carbon tape. SEM imaging of the paper precursor was carried out using a Sigma VP microscope (Carl Zeiss Microscopy, Jena, Germany) operated at an accelerating voltage of 0.7 kV with an in-lens detector. Prior to imaging, the paper precursor was coated with an approximately 3 nm thick iridium layer using an ACE600 sputter coater (Leica Microsystems, Wetzlar, Germany). The paper cross-section was obtained by manually sectioning the sample with a commercially available double edge razor blade (Wilkinson Sword, Solingen, Germany) and subsequently sputter coated and imaged under the same conditions as described prior.

2.3.6. Transmission electron microscopy (TEM)

Transmission electron microscopy (TEM) was used to examine the prepared ACs. For specimen preparation, a 300-mesh copper grid covered with a lacy carbon support film was briefly immersed in a suspension of AC in acetone (1:1000, w/w). After evaporation of the solvent, the grid was placed in the TEM holder. Imaging was performed using a JEM-2800 microscope (JEOL, Akishima, Tokyo, Japan) operated at an accelerating voltage of 200 keV, and the images were acquired with an ORIUS SC200 CCD camera (GATAN, Pleasanton, CA, USA).

2.3.7. Nitrogen adsorption experiments

Nitrogen adsorption measurements were performed at −196 °C (77 K) on a Quadrasorb SI analyzer (Quantachrome Instruments). Before analysis, ~25 mg of each specimen was degassed at 150 °C for 24 h under dynamic vacuum using a FloVac degasser. SSAs were calculated from the adsorption isotherms using the multi-point Brunauer-Emmett-Teller (BET) method in the relative pressure range p/p_0 = 0.05-0.3. Micropore surface areas were obtained with the t-plot method, while PSDs were derived by applying quenched solid density functional theory (QSDFT) for slit-shaped and cylindrical pore geometries.

2.3.8. SAXS

Small-angle X-ray scattering (SAXS) data was collected using a SAXSpoint 2.0 instrument (Anton Paar, Austria). Scattering data was collected using an Eiger 1 M detector (Dectris, Switzerland) positioned 110 and 572 mm from the sample, using a microfocused, monochromatized X-ray source Cu Kα (λ = 0.154 nm). The samples were held in the beam between two pieces of Scotch Magic tape, and the resulting data was processed using the DAWN software package, using standardized data correction procedures [40,41]. The corrected data were fit

using McSAS3, based on Monte Carlo simulations, to obtain form-free size distributions, using a spherical model [42].

3. Results and discussion

Before heating, the impregnated specimens displayed distinct wetting characteristics. At constant KOH mass, the higher water volume used for C20 results in a visible external liquid film, whereas C25 and C30 take up most of the solution and C35 retains the liquid completely within the fiber network (Fig. 3a–c, e, g). The first and largest mass-loss step at approximately 92 °C is therefore assigned to evaporation of free water (Fig. 1a–c). Consistent with the solution volumes used for impregnation, C20 shows the greatest water loss, followed by C25 and C30, while C35 shows the lowest loss (Fig. 1a–c). To compare mass changes associated with the cellulose-to-char transformation, the TGA and DTG curves were normalized at the point where heating resumed after the 60 min drying plateau (Fig. 1b–d).

MS data were recorded simultaneously with the TGA measurements for C20 and C35 (Fig. 2). For the well resolved high-temperature event in Fig. 1 d, the CO_2-MS maxima at 564–567 °C (Fig. 2c and d) occur approximately 15-18 °C above the corresponding DTG maximum at 549 °C. Such offsets can partly arise from the finite transfer time of evolved gases between the sample and the detector, which depends on the instrument geometry and carrier-gas flow rate [43].

3.1. KOH distribution after impregnation and drying

When the water volume exceeds the absorption capacity of the paper, part of the KOH solution cannot be taken up by the internal fiber network and remains on or near the sheet surface (Fig. 4). Under atmospheric impregnation conditions, this surface-associated KOH is more accessible to CO_2 and may therefore be partially converted into bicarbonate and/or carbonate species before the sample enters the tube furnace:

$$KOH + CO_2 \rightarrow KHCO_3 \quad (2)$$

$$2\,KOH + CO_2 \rightarrow K_2CO_3 + H_2O \quad (3)$$

This pre-carbonation is expected to be more pronounced in C20 than in C35 because the larger water volume in C20 exceeds the paper absorption capacity and leaves a higher fraction of KOH externally available. After the 120 °C/1 h drying step, the samples therefore differ not only in the type of K-containing species present but also in their spatial distribution. In C20, drying of the larger liquid reservoir can promote outward migration of dissolved K-species with the moving water front, followed by recrystallization at or near the surface. In C35, the lower solution volume allows more complete uptake of the KOH solution and therefore a more intimate distribution of K-species within the cellulose matrix (Fig. 4).

This difference in KOH distribution is important because potassium-catalyzed cellulose conversion is contact-dependent [31]. A more

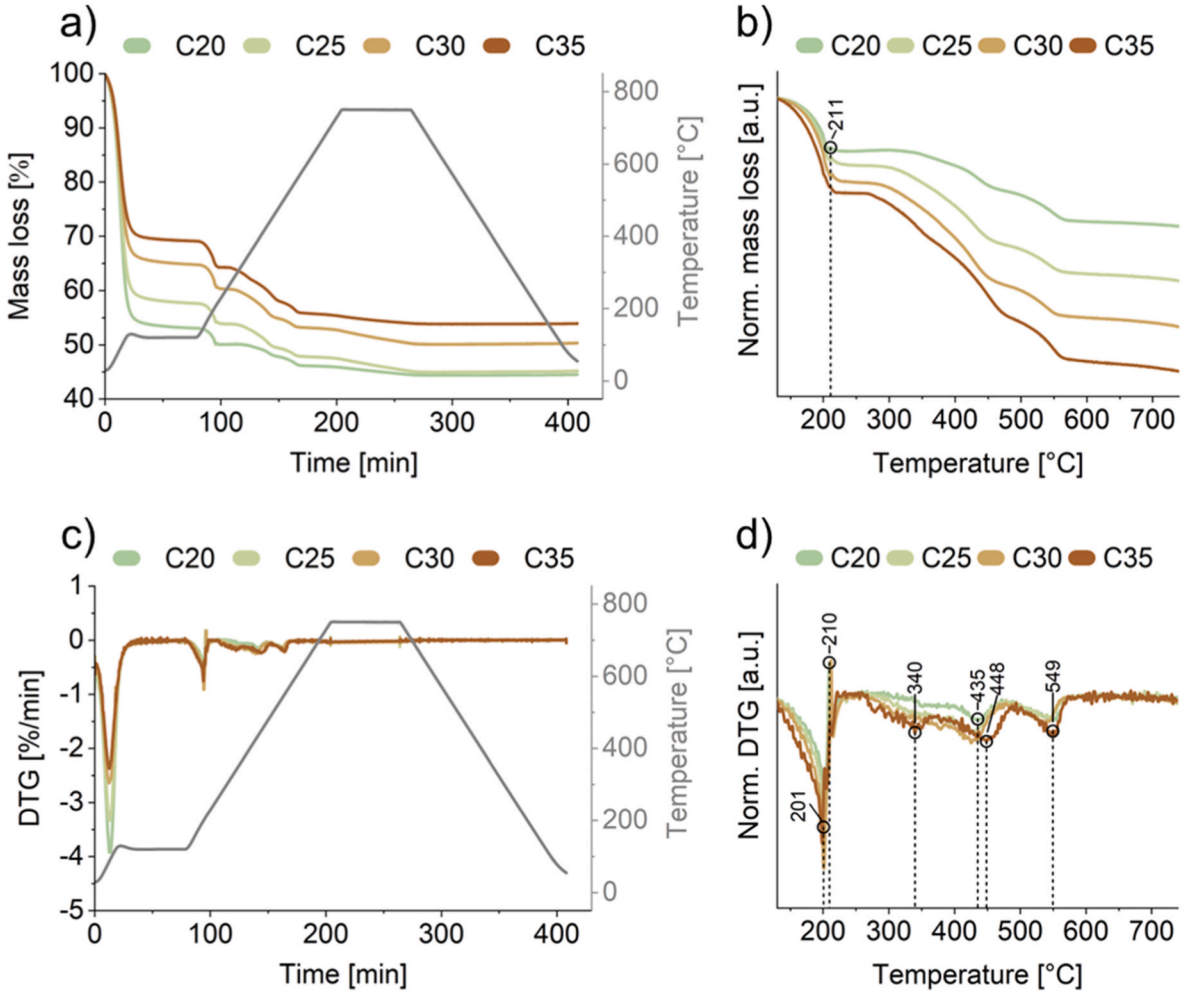

Fig. 1. TGA analysis of KOH-impregnated paper specimens: (a) total mass loss over the entire experiment and (c) the corresponding DTG curves; (b) normalized mass loss after the 1 h drying step during subsequent heating to 750 °C and (d) the corresponding DTG curves.

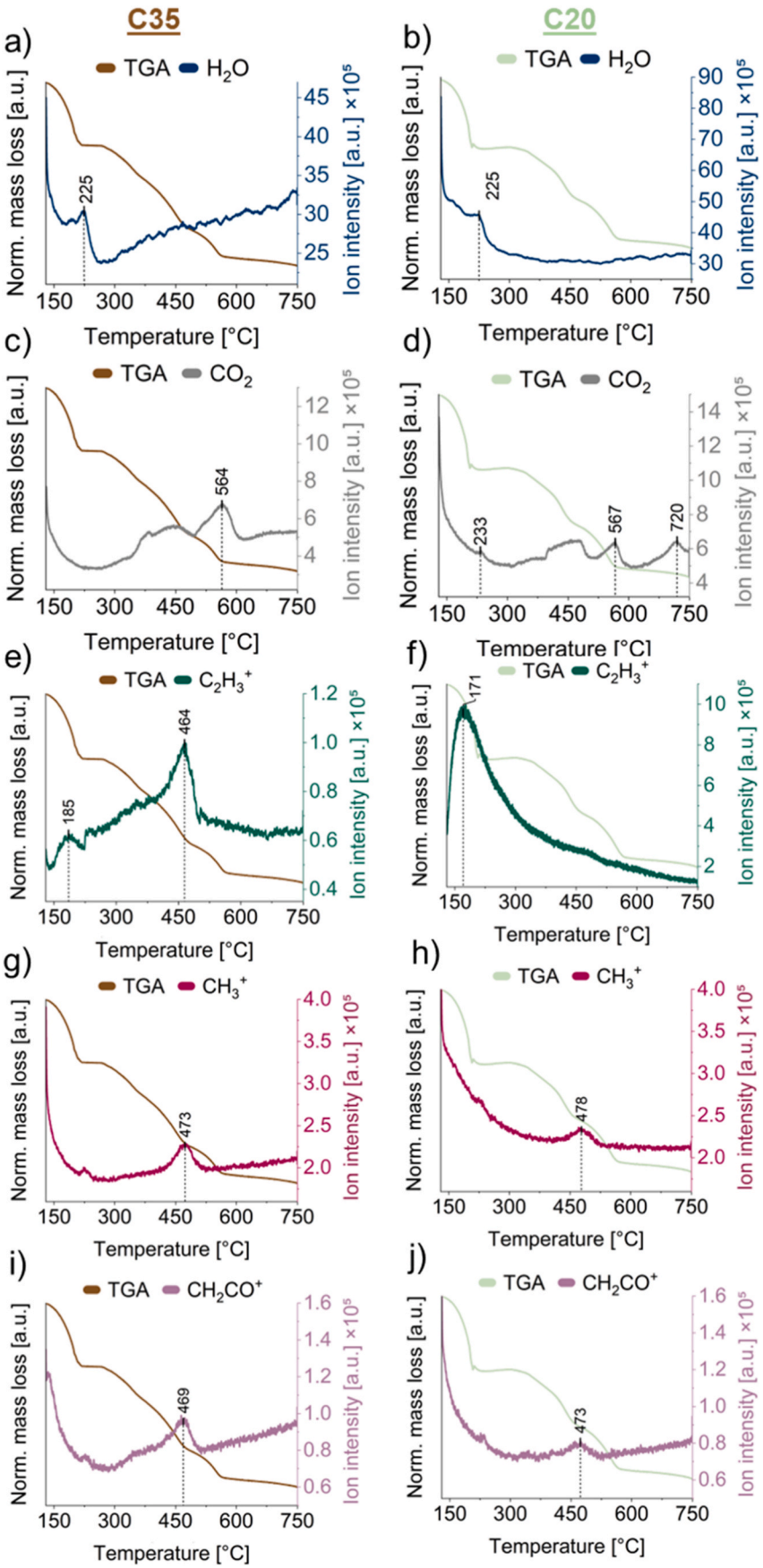

Fig. 2. TGA-MS analysis of KOH-impregnated paper specimens C35 and C20. Normalized mass loss is shown together with the corresponding MS signals for H_2O in (a,b), CO_2 in (c,d), $C_2H_3^+$ in (e,f), CH_3^+ in (g,h), and CH_2CO^+ in (i,j), with C35 shown first and C20 s in each pair.

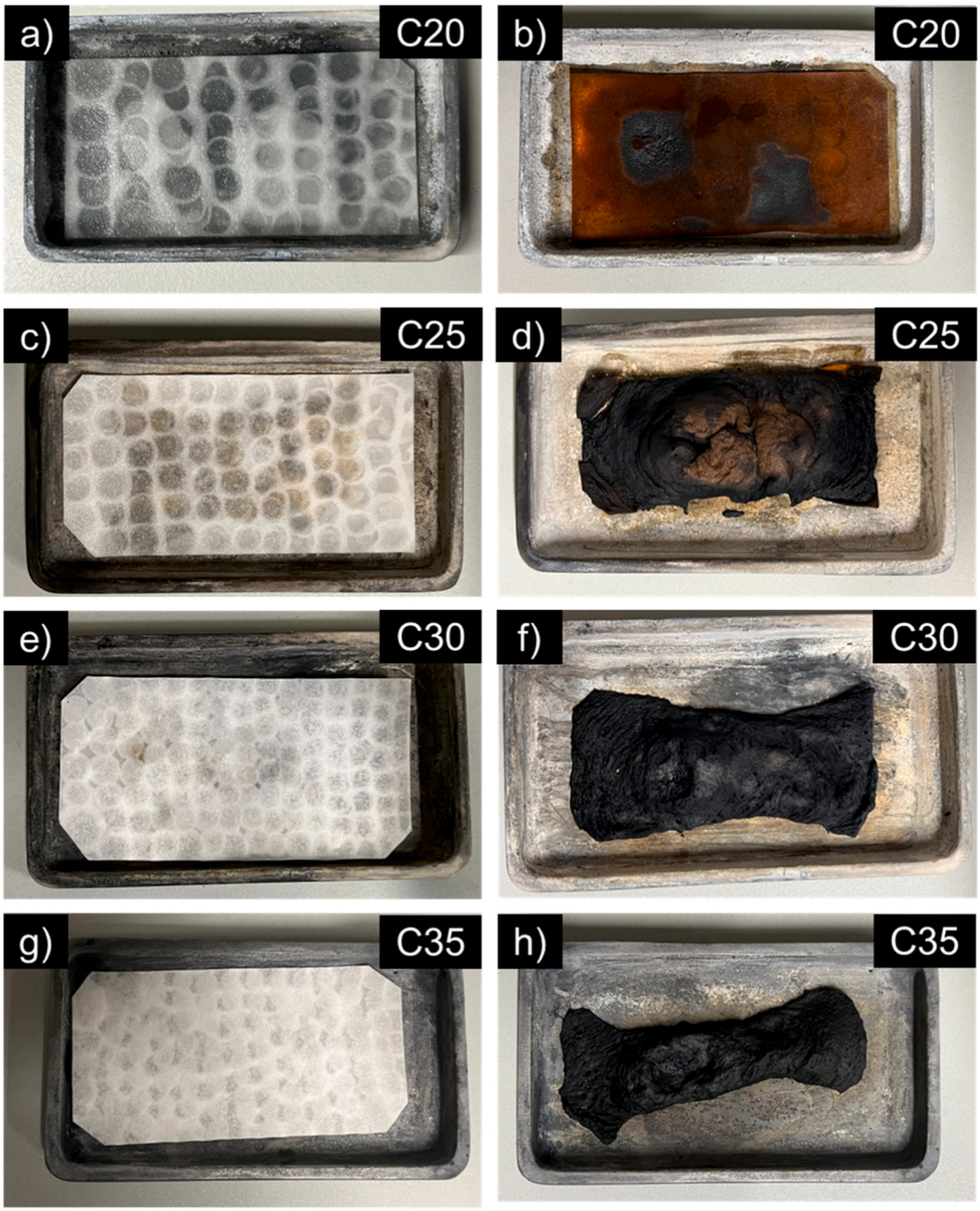

Fig. 3. Photographs of impregnated paper sheets before thermal treatment (a, c, e, g) and after isothermal drying at 120 °C and subsequent heating to 250 °C (b, d, f, h).

homogeneous KOH distribution, as expected for C35, can enhance direct KOH-cellulose interactions and promote early charring. Potassium species lower the activation barrier for cellulose degradation, causing conversion to start at substantially lower temperatures than in untreated cellulose [37,44,45]. In contrast, C20 is expected to remain in a wet, alkaline state for longer due to the higher initial water volume and the larger fraction of hygroscopic K-carbonate species, which can retain reaction-generated water. As long as water is retained in the K-rich matrix, alkaline degradation can proceed over a broader temperature range, while char stabilization is delayed.

3.2. Alkaline degradation below 250 °C

The mass-loss event associated with the DTG peak at around 201 °C is assigned to alkaline degradation (Fig. 1b–d). During this stage, KOH can participate in condensed-phase salt-forming reactions and in volatile-forming fragmentation pathways. First, KOH reacts with hydroxyl groups of cellulose or cellulose-derived fragments to form potassium alkoxides, while carboxyl-containing species are neutralized to potassium carboxylates:

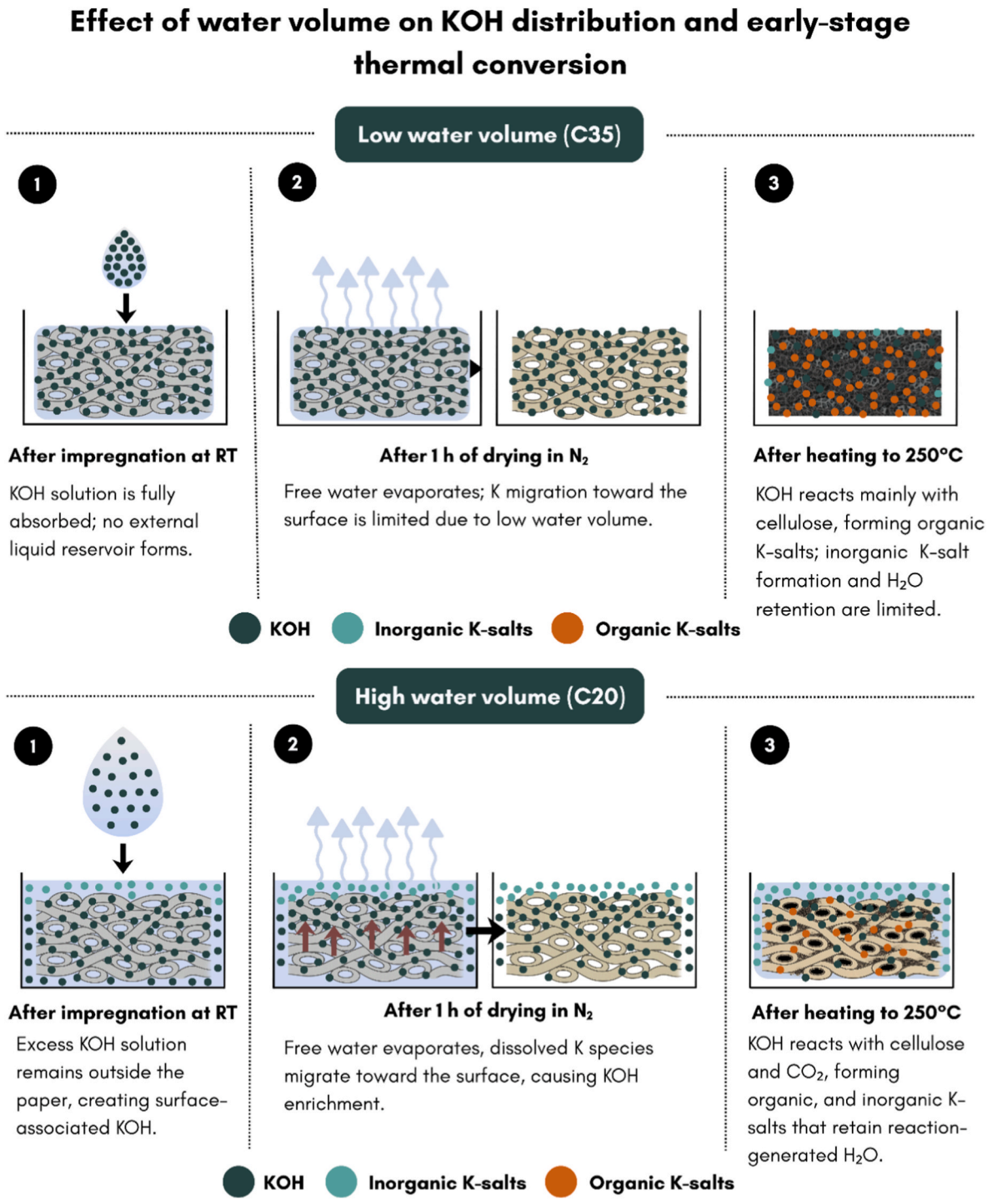

Fig. 4. Proposed influence of water volume on KOH distribution, carbonation, and the early-stage thermal conversion of KOH-impregnated paper specimens. Inorganic K-salts include $KHCO_3$ and K_2CO_3, whereas organic K-salts comprise potassium alkoxides and carboxylates.

$$R–OH + KOH \rightarrow R–O^-K^+ + H_2O \quad (4)$$

$$R–COOH + KOH \rightarrow R–COO^-K^+ + H_2O \quad (5)$$

These reactions generate reaction water and retain potassium in the condensed phase as organic K-salts. In reaction (5), R–COOH may represent pre-existing oxidized groups or carboxyl-containing products formed during alkaline degradation of cellulose.

In parallel, alkaline ring opening and isomerization of cellulose-derived glucose fragments can produce fructose/enediol-type intermediates. These intermediates can undergo retro-aldol cleavage at the C3–C4 bond to form C_3 hydroxycarbonyl intermediates such as glyceraldehyde and dihydroxyacetone [46,47]:

$$\text{open-chain } C_6 \text{ sugar fragment} \rightarrow HOCH_2–CHOH–CHO + HOCH_2–CO–CH_2OH \quad (6)$$

Glyceraldehyde is therefore considered an intermediate formed during alkaline cellulose degradation rather than a stable final product [46,47]. It can dehydrate to pyruvaldehyde [46,48]:

$$HOCH_2–CHOH–CHO \rightarrow CH_3COCHO + H_2O \quad (7)$$

Pyruvaldehyde is reported as a key intermediate that can decompose

to formic acid and acetaldehyde. In the present KOH-rich system, formic acid would be immediately converted to potassium formate [46]:

$$CH_3COCHO + KOH \rightarrow CH_3CHO + HCOOK \quad (8)$$

The CO_2-MS curves of C35 and C20 show an overall decrease in CO_2 release with increasing temperature (Fig. 2c and d). This trend is interpreted as the result of overlapping CO_2 release and CO_2 fixation processes. On the release side, preformed $KHCO_3$ generated during atmospheric impregnation can decompose upon heating to form K_2CO_3 while releasing CO_2 and H_2O:

$$2\ KHCO_3 \rightarrow K_2CO_3 + CO_2 + H_2O \quad (9)$$

The small positive CO_2 feature observed for C20 at around 233 °C suggests that CO_2 release from bicarbonate decomposition briefly exceeds the CO_2-fixation capacity of the sample in this temperature range (Fig. 2 d). This feature is not discernible for C35, most likely because less surface-associated KOH is available during impregnation and drying, so less $KHCO_3$ is expected to form (Fig. 4). Any CO_2 released in C35 may therefore be too small to resolve or may be immediately recaptured by KOH- or K-containing sites (Fig. 2 c).

On the fixation side, CO_2 can be consumed by unreacted KOH and by reactive organic K-species. Direct carbonation of KOH forms K_2CO_3 and H_2O:

$$2\ KOH + CO_2 \rightarrow K_2CO_3 + H_2O \quad (10)$$

Potassium alkoxides formed according to reaction (4) may provide additional CO_2-fixation sites. This can be represented schematically by the formation of carbonate-type potassium intermediates, consistent with reported cellulose-CO_2 reactions forming ionic cellulose carbonate species [49]:

$$R\text{–}O^-K^+ + CO_2 \rightarrow R\text{–}OCO_2^-K^+ \quad (11)$$

Both fixation pathways incorporate CO_2 into condensed K-containing species and can therefore contribute to the decreasing CO_2-MS signal (Fig. 2c and d). They may also explain the slight mass gain observed in the TGA/DTG curves at around 211/210 °C because CO_2 is incorporated into solid K-carbonate species (Fig. 1b–d). The more pronounced mass gain in C20 can be explained by stronger surface enrichment of KOH, caused by the solution volume exceeding the paper's absorption capacity, which increases the availability of K-containing sites for CO_2 fixation.

The H_2O-MS signal also decreases overall in both samples and reflects the balance between reaction-water formation, water release into the gas phase, and water retention by hygroscopic K-containing species (Fig. 2a and b). The decreasing H_2O signal suggests that a considerable fraction of newly formed water is retained within the K-rich matrix, particularly by K_2CO_3 and related carbonate species. The transient deviation from this trend, with a peak around 225 °C, indicates that water release temporarily exceeds the retention capacity of the sample (Fig. 2a and b). This H_2O increase can arise from $KHCO_3$ decomposition, direct carbonation of unreacted KOH to K_2CO_3, and KOH-cellulose reactions forming organic K-salts. After this event, the H_2O signal decreases again, indicating depletion of the available water-generating sources and/or renewed retention of water by newly formed K-carbonate species.

The different shapes of the H_2O shoulders further support the proposed difference in K-species distribution (Fig. 2a and b). In C20, the deviation from the decreasing signal starts earlier and extends over a broader temperature range, indicating gradual water release from a heterogeneous, surface-enriched K environment (Fig. 2 b). This is consistent with enhanced CO_2 fixation, increased potassium carbonate formation, and stronger water retention. In C35, the deviation occurs later and appears more pronounced, suggesting a more localized release event that is consistent with fewer carbonate-rich surface domains and more confined KOH-cellulose interactions within the paper structure (Fig. 2 a).

3.3. Organic fragments below 250 °C

The water-volume-dependent differences in alkaline degradation below 250 °C become even clearer when the MS release patterns of organic fragments are considered (Fig. 2e–j). The signals at $m/z = 27$, 15, and 42 have been assigned in the literature to $C_2H_3^+$, CH_3^+, and CH_2CO^+, respectively [50]. All three ions can originate from acetaldehyde formed during secondary alkaline degradation. Acetaldehyde is expected to fragment in the EI source of the MS at 70 eV according to several pathways, including [50]:

$$CH_3CHO \rightarrow C_2H_3^+ + OH \quad (12)$$

$$CH_3CHO \rightarrow CH_3^+ + HCO \quad (13)$$

$$CH_3CHO \rightarrow CH_2CO^+ + H_2 \quad (14)$$

The most characteristic acetaldehyde fragment would be CHO^+ at $m/z = 29$. However, $m/z = 29$ cannot be used here as an independent acetaldehyde marker because nitrogen also contributes at this mass through naturally occurring nitrogen isotopologues [51]. In the present measurements, the continuously supplied N_2 carrier gas produced a strong background in this mass region, preventing an unambiguous assignment to CHO^+. Therefore, $m/z = 29$ was not used for product assignment or interpretation and is not shown.

$C_2H_3^+$ exhibits a pronounced maximum at 171 °C in C20, followed by a continuous decrease with increasing temperature (Fig. 2 f). In the same temperature region, CH_3^+ and CH_2CO^+ are also detected (Fig. 2h–j), although their profiles do not scale directly with $C_2H_3^+$. This indicates that the three signals cannot be interpreted as a simple one-to-one fingerprint of a single volatile precursor. Differences in ion formation and detection for the individual m/z channels or overlapping contributions from several low-molecular-weight volatiles may contribute to the observed pattern. Independent of the exact origin, the much stronger $C_2H_3^+$ signal together with the slightly stronger CH_3^+ signal demonstrates that C20 releases more low-molecular-weight organic fragments in this temperature region than C35 (Fig. 2e–h). This provides further evidence that alkaline degradation is more pronounced in C20 as a consequence of the larger water volume used for impregnation.

The visual appearance of the samples after heating to 250 °C further supports the proposed differences in early-stage conversion. C35 is already fully black, whereas C30, C25, and particularly C20 exhibit progressively lower degrees of carbonization. The C20 surface remains brown, while shrinkage increases systematically from C20 to C35 (Fig. 3b–d, f, h). This behavior is consistent with prolonged alkaline degradation and delayed char formation in C20.

3.4. Formation of a carbon-rich and aromatic char structure above 250 °C

C20 enters this temperature stage with a more hydrated, carbonate-rich, and less carbonized structure because the larger initial water volume prolongs wet alkaline degradation. In contrast, C35 has already undergone more extensive drying and earlier char formation. As heating proceeds, the K-rich condensed phase becomes progressively less hydrated because water-generating reactions are depleted and released water is continuously removed. The decreasing mobility of the alkaline phase slows further alkaline degradation and favors condensation, dehydration, and crosslinking of cellulose-derived products retained in the solid phase. Consequently, the transition from an oxygen-rich brown intermediate to a more aromatic black char occurs earlier in C35 and is delayed in C20 (Fig. 3b–d, f, h).

The subsequent DTG peak at 340 °C, with an onset at approximately 260 °C, is assigned to further transformation of the already formed char (Fig. 1b–d). At this stage, the char still contains residual oxygen-containing groups formed during the initial reactions between the precursor and KOH. These groups can undergo dehydration,

decarboxylation, deoxygenation, and condensation reactions, removing oxygen from the condensed phase mainly as H_2O, CO_2, and CO and producing a more carbon-rich and aromatic char structure. In parallel, residual KOH can dehydrate to K_2O, a transformation reported to begin around 300 °C when excess KOH is present [31,39]. As the temperature approaches the melting point of KOH at 360 °C, a mobile KOH-rich ionic phase can form. This phase may also contain potassium oxide and other potassium species, facilitating contact with the evolving char. Evolving gases may become partially retained within the melt, promoting interconversion among KOH, K_2O, and K_2CO_3 [16].

The MS signals provide further insight into the progression of char maturation (Fig. 2a–d). For C35, the H_2O signal increases steadily after approximately 260 °C and continues to rise until the end of carbonization (Fig. 2 a). In contrast, the H_2O signal of C20 remains nearly constant over the same temperature range (Fig. 2 b). This suggests that part of the generated water is retained within the K-rich melt. The prolonged water retention in C20 maintains a more hydrated alkaline environment for a longer time and slows charring, explaining why C20 carbonizes more slowly than samples impregnated with lower KOH solution volumes. The CO_2-MS signal also reflects this delayed transformation: for C35, CO_2 release increases above approximately 264 °C, whereas the corresponding increase in C20 starts only at approximately 309 °C (Fig. 2c and d). This shift to higher temperature indicates that the removal of residual oxygen-containing groups from the char occurs earlier in C35 but is delayed in C20.

3.5. High-temperature organic fragment release

For all organic fragment signals, except for $C_2H_3^+$ in C20 where the low-temperature maximum is dominant, a second release maximum is observed at approximately 470-480 °C (Fig. 2e–j). These maxima coincide with a stronger mass-loss peak for C35 at 448 °C than for C20 at 435 °C, indicating that more material retained in the solid phase of C35 decomposes and is released as volatile products in this temperature range. This behavior can be linked to the different pathways established by the initial water volume. In C20, the larger water volume prolongs wet alkaline degradation and promotes the release of a substantial fraction of cellulose-derived material already below 250 °C. Consequently, less condensed organic material remains available for release at 470-480 °C. In C35, the lower water volume promotes earlier char formation and preserves a larger fraction of the cellulose-derived material within the condensed phase. The resulting oxygen-rich char and retained organic potassium intermediates subsequently undergo decomposition and deoxygenation, producing the stronger mass loss and more clearly resolved organic-fragment maxima observed in this temperature region.

The high-temperature organic fragment release may include acetaldehyde release, which generates $C_2H_3^+$, CH_3^+, and CH_2CO^+ in the EI source according to reactions (12)-(14). At these temperatures, acetaldehyde formation by wet alkaline degradation is unlikely. Instead, it may originate from the decomposition of organic potassium salts. A representative example is potassium lactate, since lactic acid is reported as a major product of alkaline cellulose degradation [46]. In the KOH-rich environment, lactic acid would mainly be present as potassium lactate, which can decompose further during heating. A possible conversion is proposed schematically as:

$$CH_3CH(OH)COOK + KOH \rightarrow CH_3CHO + K_2CO_3 + H_2 \quad (15)$$

In the same temperature region, residual KOH can also begin to attack the newly formed carbon framework directly [20]:

$$6KOH + 2C \rightarrow 2K_2CO_3 + 2K + 3H_2 \quad (16)$$

This temperature stage represents therefore a transition from the conversion of retained oxygen-containing and organic potassium intermediates to direct activation of the carbon framework. Its greater intensity in C35 is consistent with the larger amount of condensed material preserved by earlier char formation, whereas the prolonged wet degradation pathway in C20 removes more material during the preceding low-temperature stage.

3.6. CO_2 evolution above 500 °C and late K_2CO_3-assisted activation

Once KOH is largely consumed and converted into K_2CO_3, CO_2 is no longer effectively captured and is instead released. This gives rise to the DTG peak near 549 °C and the corresponding CO_2-MS maxima at 564 °C for C35 and 567 °C for C20 (Fig. 1 d; Fig. 2c and d). Beyond this region, the CO_2 signal decreases, which is consistent with partial consumption of CO_2 by the carbon matrix via the Boudouard reaction ($CO_2 + C \rightarrow 2$ CO).

In contrast to C35, C20 shows a second CO_2 maximum at approximately 720 °C, indicating an additional high-temperature activation event (Fig. 2 d). This difference is linked to the initial water content and the resulting early-stage conversion pathway. The larger solution volume in C20 promotes a prolonged wet alkaline environment and delayed char formation. Consequently, C20 reaches the high-temperature region with a char structure that still contains many oxygen-containing groups. In C35, the lower water volume allows earlier char formation and earlier deoxygenation, so fewer reactive C–O and C═O sites remain available at approximately 720 °C. The CO_2 peak around 720 °C is therefore attributed to the interaction of K_2CO_3 with oxygen-containing groups in the char. The relevant reactions proposed for CO_2 formation are [52]:

$$K_2CO_3 + 2\ C\text{–}O \rightarrow K_2O\text{–}C + 2\ CO_2 \quad (17)$$

$$K_2CO_3 + 2C{=}O \rightarrow K_2O\text{–}C + 2\ CO_2 \quad (18)$$

Accordingly, the pronounced peak in C20 reflects the simultaneous availability of K_2CO_3 and oxygen-containing char sites, whereas the absence of a distinct peak in C35 is consistent with earlier char maturation and more extensive prior deoxygenation. During this late activation step, oxygen-containing carbon sites are removed as CO_2, while K_2O-containing carbon complexes are formed. The released CO_2 may subsequently gasify the carbon matrix through the Boudouard reaction, contributing to additional carbon loss and pore widening in C20.

3.7. Integrated MS response during the heating ramp

To compare the overall MS response during the heating ramp, the areas under the selected MS signals were integrated from 130 °C to the first data point at which 750 °C was reached, excluding the isothermal drying and activation holds (Fig. 5). Both TGA-MS measurements were performed using 20 mg of paper precursor and, because the KOH-to-precursor mass ratio was fixed at 1:1, the same dry KOH mass. The integrated signal areas can therefore be compared directly on an equal precursor and KOH mass basis. However, they do not represent absolute product yields and permit only a semi-quantitative comparison. At the start of the integration at 130 °C, the water originally introduced with the impregnation solution had already been completely removed during the preceding 1 h drying step at 120 °C. The integrated H_2O signal therefore reflects the release of water generated during thermal reactions or temporarily retained within the K-rich phase. C20 exhibits higher integrated areas for H_2O, CO_2, $C_2H_3^+$, and CH_3^+ than C35, whereas the CH_2CO^+ area is slightly higher for C35 (Fig. 5). The largest difference among the organic fragment signals is observed for $C_2H_3^+$, whose integrated area is approximately 5.4 times higher for C20. These results indicate that the larger water volume used for C20 leads to greater release of MS-detected species. This further supports a more pronounced alkaline degradation stage and greater carbon loss to the volatile phase.

ATR-FTIR spectra of the KOH-impregnated sheets after treatment at 250 °C (Fig. 6) differ fundamentally from those of untreated cellulose. The characteristic cellulose fingerprint bands previously identified for this precursor paper in our earlier work [1] (1426, 1364, 1333, 1314,

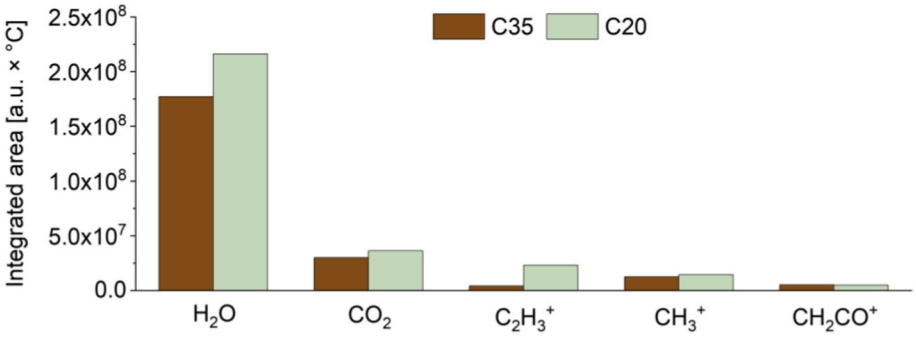

Fig. 5. Integrated areas of MS signals for C20 and C35 from 130 °C to 750 °C, excluding the isothermal drying and activation holds. The values allow a semi-quantitative comparison of volatile-release intensity but do not represent absolute product yields.

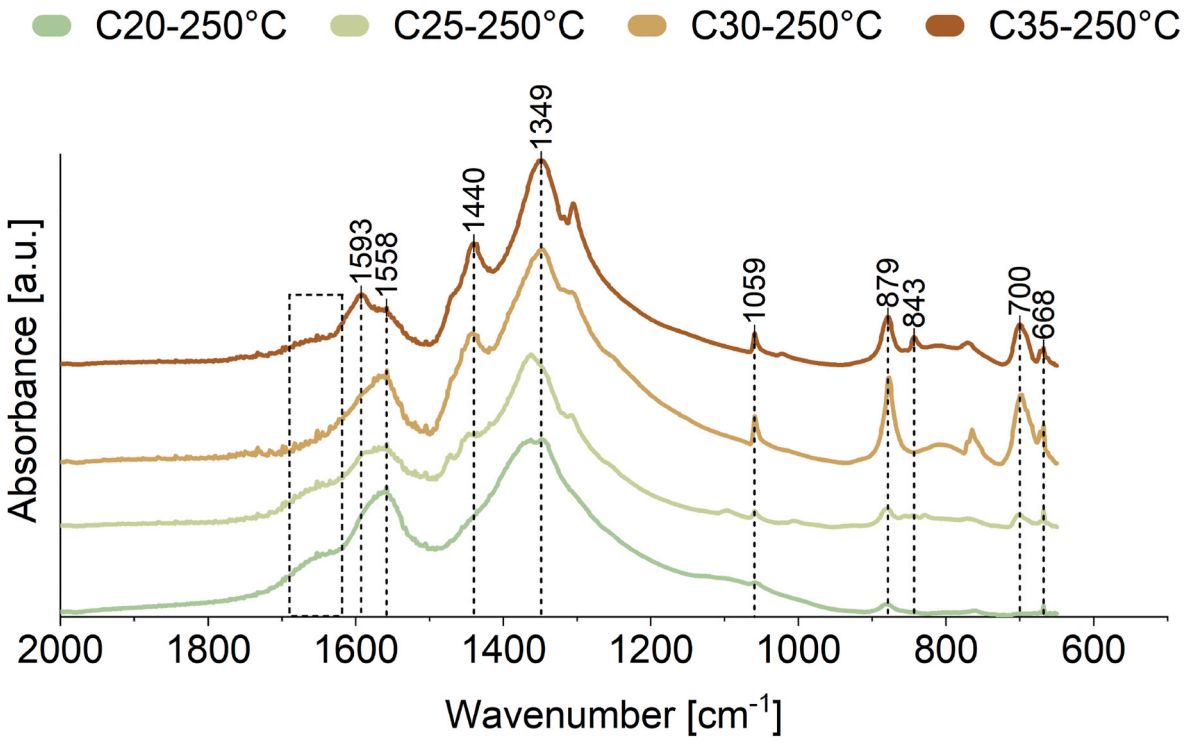

Fig. 6. ATR-FTIR spectra of the impregnated paper sheets after isothermal drying at 120 °C and subsequent heating to 250 °C.

1200, 1159 cm^{-1}), as well as the 1103-1000 cm^{-1} region and the β-glycosidic band at 896 cm^{-1}, are not observed here, indicating that the probed surface is no longer dominated by intact cellulose. However, carbohydrate-derived intermediates formed during the initial charring of cellulose (polyfuranic/humin-like structures) likely contribute to the remaining broad absorption envelope with a local maximum at ~1349 cm^{-1} [44].

Instead, the spectra are dominated by a set of bands consistent with the formation of an incipient carbonaceous structure together with a substantial contribution from inorganic carbonate species. The bands at 1593 and 1558 cm^{-1} lie in a region assigned to aromatic C=C skeletal stretching in thermally converted lignocellulosic materials, indicating progressive aromatization during treatment [45]. The presence of carbonate is evidenced by the band at 1440 cm^{-1}, attributed to the ν_3 asymmetric C–O stretching of CO_3^{2-}, together with the band at 1059 cm^{-1}, which falls within the range reported for the ν_1 symmetric C–O stretching of carbonate species [53]. The bands at 879 and 843 cm^{-1} are assigned to the ν_2 out-of-plane bending mode of carbonate. The additional component at 843 cm^{-1} may arise from ν_2 splitting or from carbonate species in non-equivalent local environments [54]. Its resolution in C35 therefore reflects local heterogeneity, which may stem from differences in hydration state (e.g., coexistence of less hydrated and more strongly hydrated carbonate species), but could also be related to variations in coordination, ion pairing, or structural disorder. The bands observed at 700 and 668 cm^{-1} are attributed to the ν_4 in-plane bending mode of carbonate [55]. In addition, the shoulder around 1630 cm^{-1} can be attributed to adsorbed water [56].

Peak resolution increases from C20 to C35, even though C35 is visually more carbonized. ATR-FTIR probes only the first micron-scale region in close contact with the crystal, and in wet media the measured spectrum is dominated by an interfacial water film with only a weak contribution from the solid. Accordingly, the wetter C20 exhibits stronger water-film masking, and a higher fraction of potassium species remain dissolved rather than precipitated at the surface, both of which diminish apparent band intensities and blur fine spectral features. In contrast, the more carbonized specimens (C30 and C35) present a drier, more rigid surface with surface-precipitated carbonate species, resulting in sharper and more intense carbonate- and aromatic-related bands.

The XRD diffractograms of the KOH-treated, thermally converted sheets (Fig. 7) deviate strongly from that of the precursor paper,

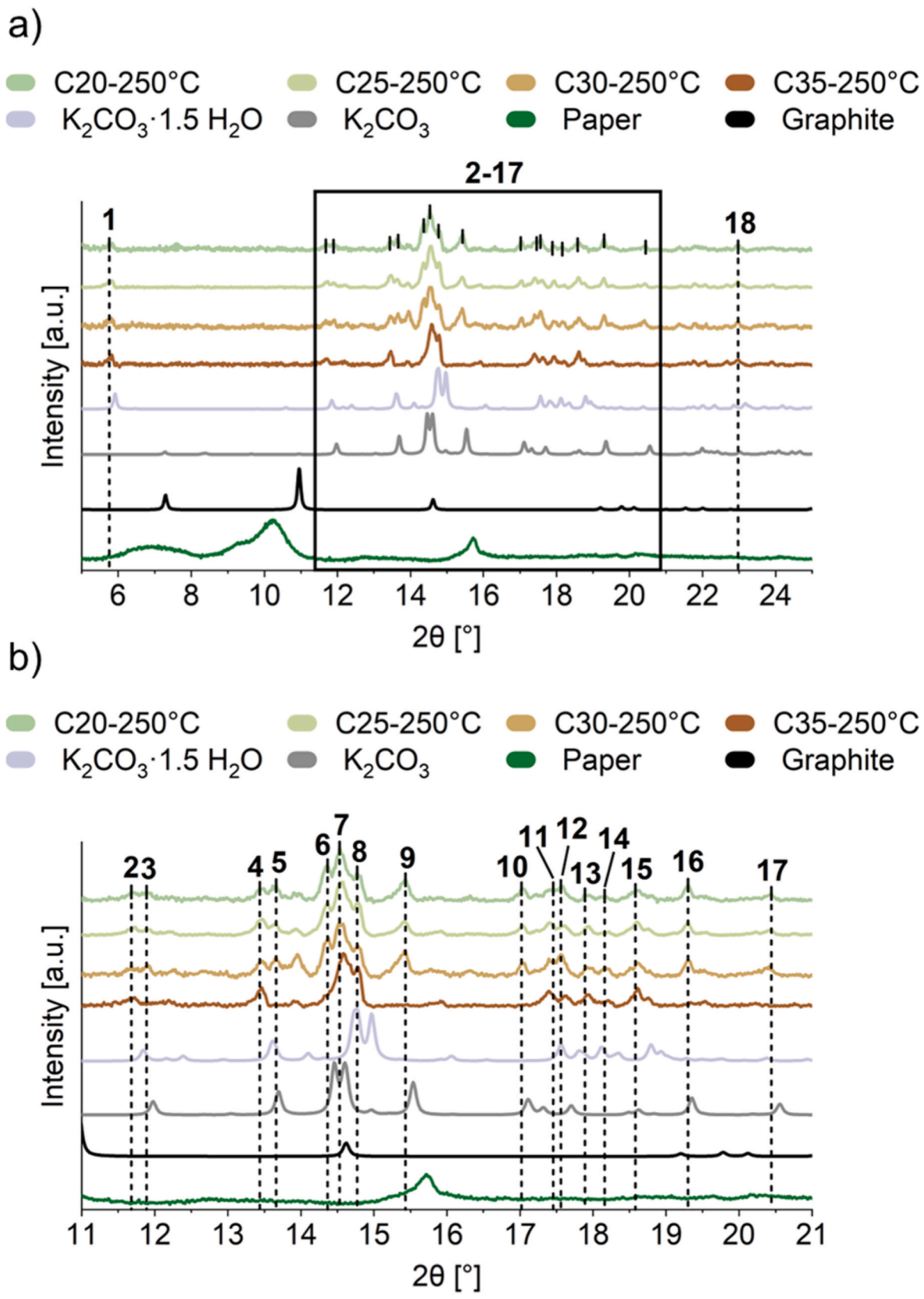

Fig. 7. (a) Stacked XRD patterns of KOH-impregnated paper sheets after drying (120 °C, 1 h) and subsequent heating to 250 °C (C20–C35_250 °C), compared with untreated paper and simulated reference patterns of potassium carbonates ($K_2CO_3{\cdot}1.5H_2O$ and K_2CO_3) and graphite (all simulated from CIF files [57–59]). (b) Enlarged view of the highlighted 2θ region; corresponding 2θ positions are listed in Table S1.

indicating that the native cellulose structure is largely lost already at 250 °C. This is consistent with the pronounced optical changes observed after thermal treatment (Fig. 3).

C20–C35_250 °C exhibit numerous reflections across 2θ ~ 5-25° (Fig. 7 a), with the expanded view highlighting a particularly peak-rich region between ~12 and 21° (Fig. 7 b). These reflections overlap with potassium carbonate reference patterns ($K_2CO_3 \cdot 1.5H_2O$ and K_2CO_3). This assignment agrees with the ATR-FTIR results (Fig. 6), where carbonate vibrational bands dominate the spectra. Within the series, C20–C30_250 °C display similar peak sets with only minor peak position offsets, suggesting small variations in carbonate hydration state and/or crystallinity. In contrast, C35 lacks several reflections present in C20–C30_250 °C (e.g., peaks 3, 5, 6, 9, 16, and 17 in Fig. 7 b; exact 2θ positions are listed in Table S1), indicating either a modified salt mixture or altered phase proportions. Since these salts are hygroscopic, differences in ambient exposure and sample handling may have contributed to the apparent disappearance of reflections in C35_250 °C.

No distinct graphite-related reflections are observed in C20–C35_250 °C. This is expected because treatment at 250 °C does not produce considerable graphitic order; any carbon formed at this stage is largely amorphous and would contribute only a broad, low-intensity background feature rather than sharp peaks.

The carbon yield decreases with increasing KOH solution volume used for precursor impregnation (Fig. 8, a), with the yield of C35 being nearly an order of magnitude higher than that of C20. The generally low yields (<10%) are typical for the one-step KOH activation process, since the yield is calculated relative to the mass of the original precursor rather than a pre-carbonized intermediate, and because cellulosic precursors undergo extensive chemical etching due to their highly reactive functional groups.

Alkaline degradation, during which anhydroglucose units are removed from the cellulose backbone and converted into volatile degradation products, proceeds for a longer time in specimens impregnated with higher KOH solution volumes. These specimens remain wet for a longer period of time, delaying the onset of carbonization to higher temperatures (Fig. 3b–d, f, h). Consequently, a larger fraction of the original cellulose is converted into non-carbonizing degradation products in C20. This interpretation is supported by the integrated MS response during the heating ramp, which shows higher total signal areas for H_2O, CO_2, $C_2H_3^+$, and CH_3^+ in C20 than in C35, with the $C_2H_3^+$ area being approximately 5.4 times higher (Fig. 5). Although these integrated values are only semi-quantitative, they demonstrate enhanced volatile release from C20 and therefore support a stronger loss of carbon-containing species before char stabilization.

With decreasing KOH solution volume, the duration of alkaline degradation decreases and aromatization begins earlier, preserving a larger fraction of the cellulose backbone that subsequently forms the carbon matrix. This explains the increase in carbon yield from C20 to C35. In addition, the CO_2-MS signal indicates that C20 undergoes an additional high-temperature CO_2-associated activation step at approximately 720 °C (Fig. 2 d). During this process, CO_2 can react with the carbon matrix, further contributing to carbon loss and thus to the lower yield of C20.

The K-salt residues on the unwashed ACs (Fig. 8 b) originate from reactions of KOH with CO_2 and H_2O during thermal treatment. A decreasing trend in K-salt content is observed with decreasing KOH solution volume. However, the difference in salt mass between C20 and C35 is only about 5%, which is unexpected considering the pronounced visual differences in the unwashed ACs (Fig. 8c and d). While C35 appears uniformly black with a foam-like texture, C20 exhibits a black carbon core surrounded by a white crust of K-salts. This contrast indicates that the applied KOH solution volume controls whether potassium salts form predominantly as external crusts or remain more uniformly distributed within the carbon matrix after activation. In C35,

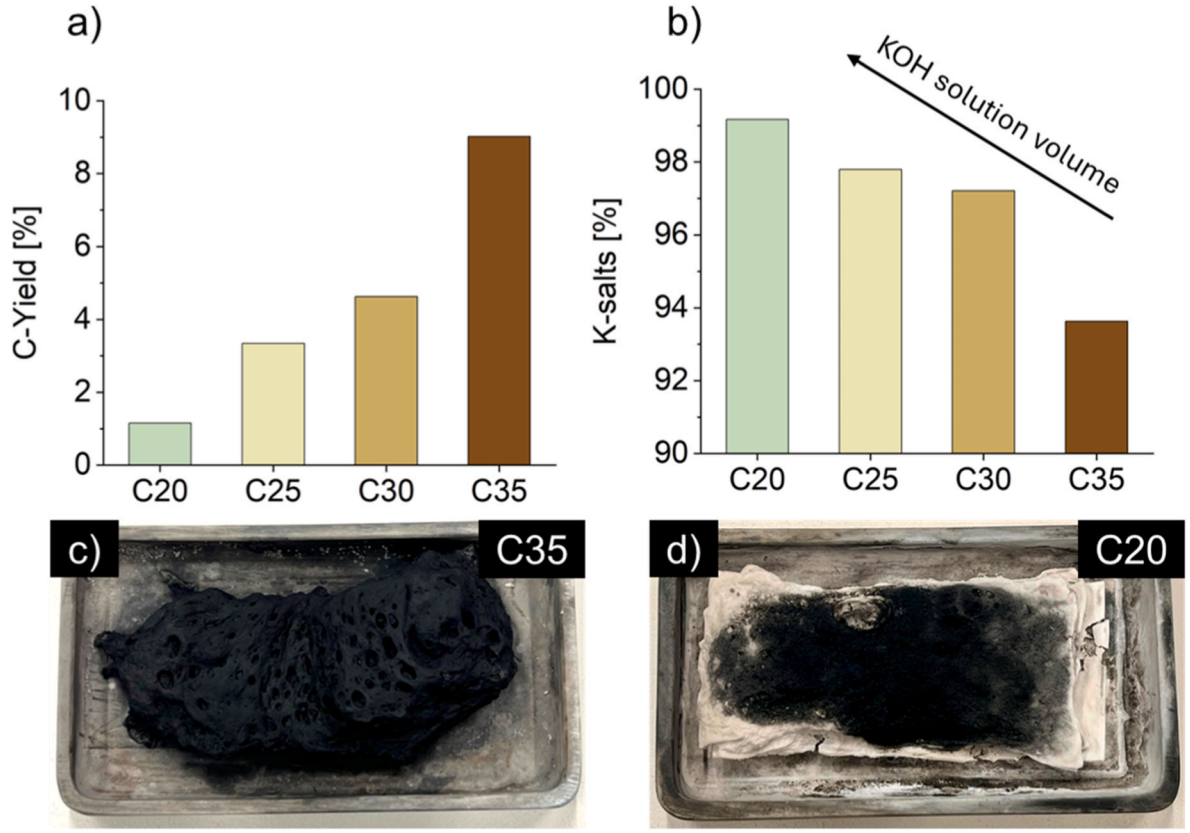

Fig. 8. (a) Carbon yield relative to precursor mass, (b) Fraction of K-salts calculated from the masses of washed and unwashed AC, and images of unwashed ACs produced with 35 w.% (c) and 20 w.% (d) KOH solution.

the entire solution volume is absorbed into the precursor paper, resulting in potassium-salt formation predominantly within the bulk. In C20, the applied solution volume is almost twice the uptake limit. Assuming an initially homogeneous solution, nearly half of the applied KOH is therefore in the external liquid fraction before drying. Moreover, evaporation during drying may induce outward solvent transport, carrying dissolved potassium species from the sheet interior toward the evaporation front (Fig. 4). This efflorescence-like redistribution could

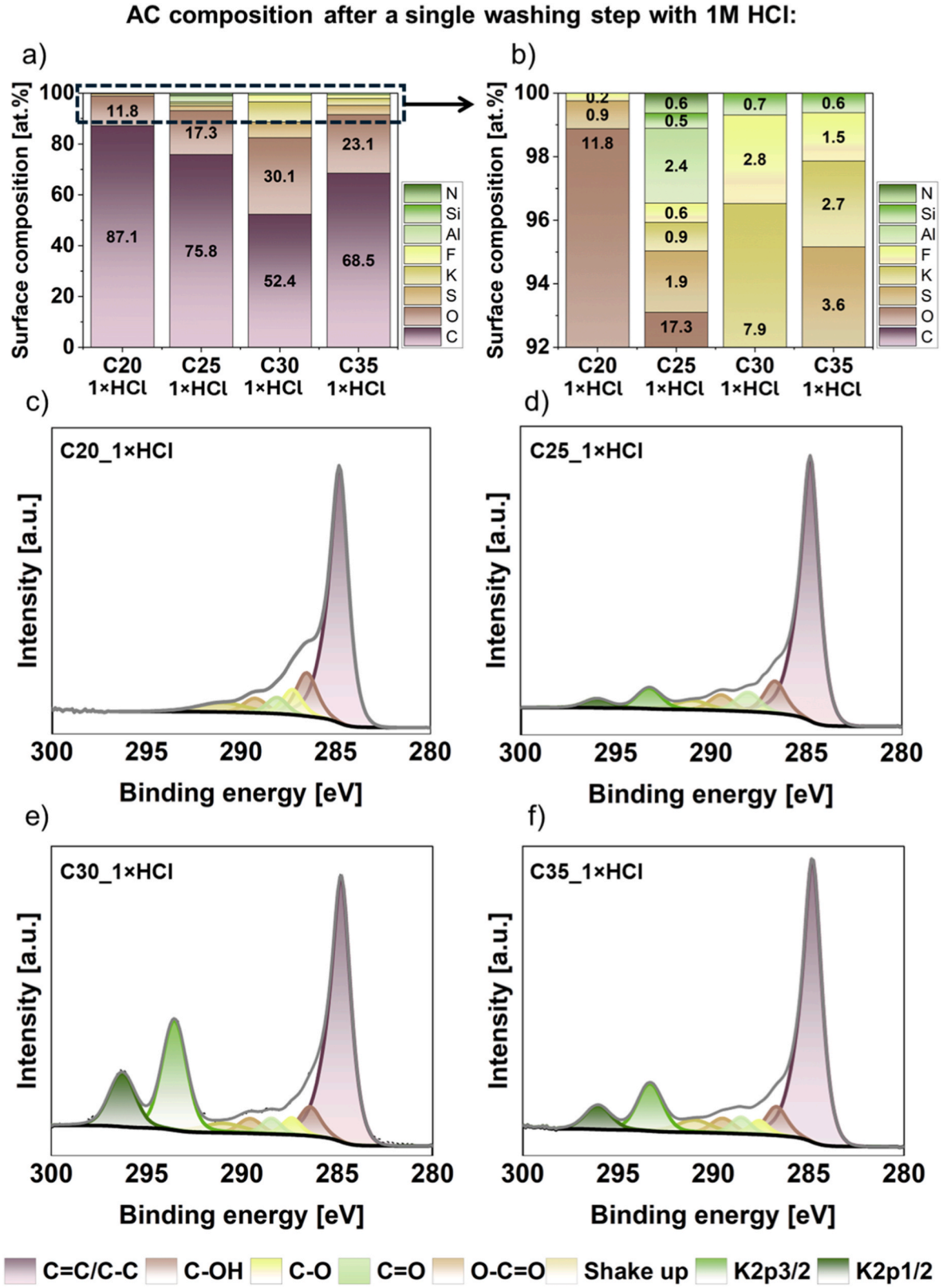

Fig. 9. (a, b) Surface atomic composition obtained by XPS for AC samples (C20–C35) after one HCl wash. (c-f) High-resolution C 1s spectra and corresponding peak fitting showing the contributions of different carbon functional groups for C20, C25, C30, and C35.

further increase the surface-associated KOH fraction in C20. Such redistribution is expected to be less pronounced in C35 because its smaller liquid reservoir is removed more rapidly and a continuous aqueous phase is maintained for a shorter period. During subsequent thermal treatment, the surface-enriched potassium species in C20 are converted mainly into K_2CO_3, producing the pronounced external salt crust observed in Fig. 8 d.

XRD analysis of the unwashed C20 and C35 ACs further supports this difference in salt distribution (Fig. S2). Both patterns contain reflections associated with K_2CO_3 and $K_2CO_3{\cdot}1.5H_2O$. However, the substantially sharper and more intense reflections of C20 indicate larger and more crystalline salt domains in the external crust, whereas the weaker and less resolved reflections of C35 are consistent with smaller or more disordered crystallites confined within the carbon structure [60]. Differences in the relative peak sets may additionally reflect variations in carbonate hydration state and phase proportions.

XPS probes the near-surface elemental composition and is therefore highly sensitive to trace residues and surface contamination. For the present ACs (Figs. 9 and 10, a, b), C represents the carbon matrix. O arises from oxygen-containing surface functionalities generated during KOH activation and from oxygen containing inorganic residues such as K_2CO_3. Residual K is attributed to activator-derived potassium species that are not fully removed by a single washing step, including K–O surface complexes and potassium salts (e.g., carbonates). Trace S is consistent with the acid sulfite origin of the cellulose fibers, whereas Si and Al likely reflect minor ash/mineral impurities (e.g., aluminosilicates). Fluorine is not expected to originate from either the cellulose precursor or the activation chemistry. Its presence therefore suggests contamination from an external fluorine-containing source introduced during processing, potentially from the sealing rings of the tube furnace. N may originate from trace precursor residues and/or adsorption.

The changes induced by the second washing step in the AC surface composition (Fig. 10a and b) indicate that a substantial fraction of the XPS oxygen signal originates from oxygen-containing potassium residues. After the second wash, the surface oxygen content decreases strongly (C30_1×HCl: 30.1 → C30_2×HCl: 10.6 at.%; C35_1×HCl: 23.1 → C35_2×HCl: 12.3 at.%). Potassium and contaminations such as Si, Al, and F are no longer detected. This behavior is consistent with the dissolution of residual K-salts and their associated oxygen species and is further supported by the disappearance of K-related contributions in the high-resolution spectra (Fig. 10c and d). As a result, the surface compositions of C30_2×HCl and C35_2×HCl converge to very similar values (O ~ 11-12 at.%, S ~ 0.3-0.4 at.%, N ~ 0.5 at.%). These observations indicate that the elevated oxygen contents measured after the first wash were largely due to removable oxygen-containing K residues. With K being removed, the C 1s envelope is dominated by the carbon scaffold

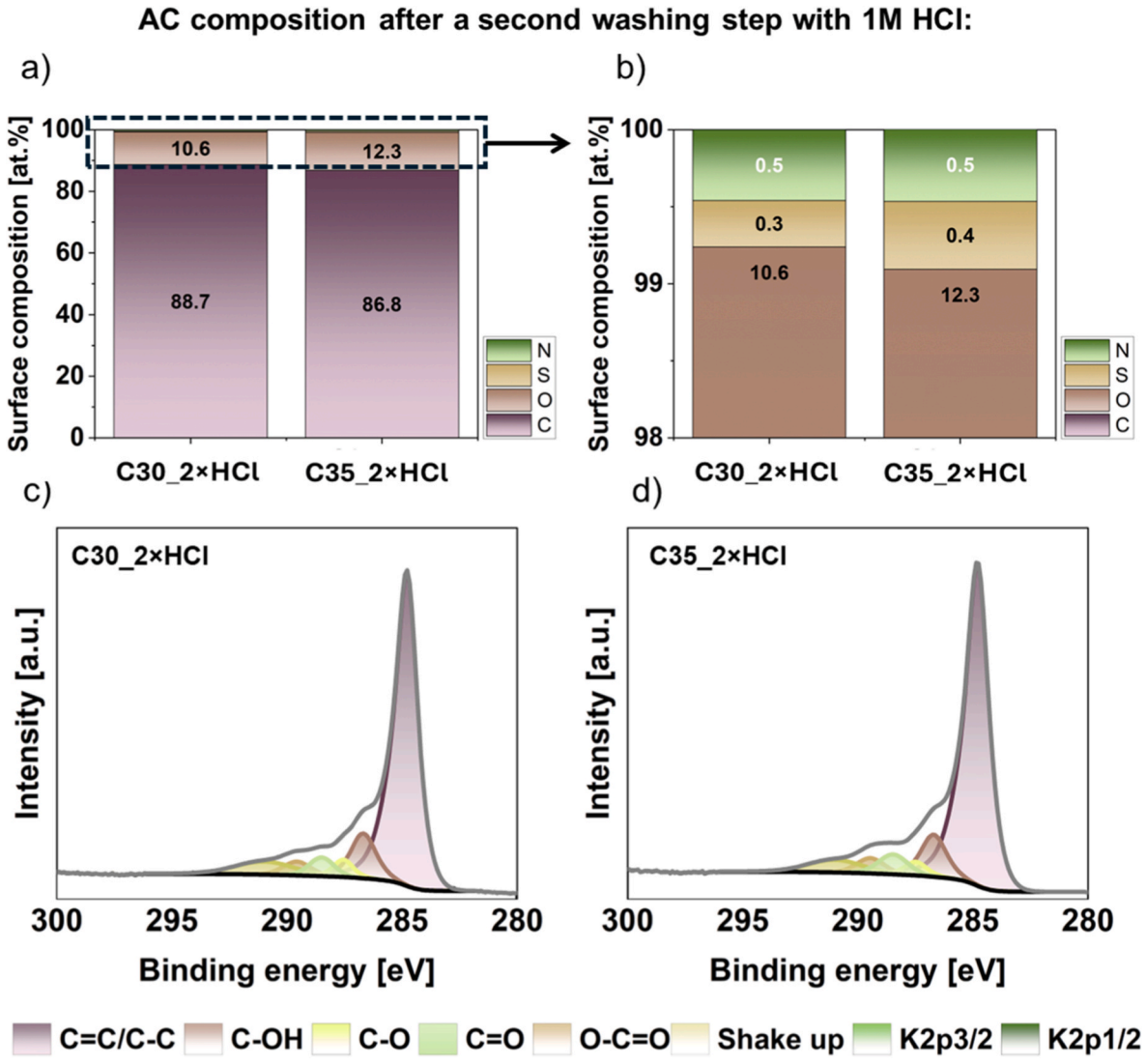

Fig. 10. (a, b) Surface atomic composition obtained by XPS of C30 and C35 after a second HCl wash. (c, d) High-resolution C 1s spectra and corresponding peak fitting showing the contributions of different carbon functional groups for the rewashed C30 and C35.

(C–C/C═C), together with a smaller but distinct contribution from covalently bound oxygen functional groups, mainly C–OH/C–O with minor C═O and O–C═O components (Fig. 10c and d).

The AC atomic composition after the first and second wash (Figs. 9 and 10a and b) are consistent with the visually observed differences in potassium-salt distribution in the unwashed specimens (Fig. 8c and d). For C20, photographs show a superficial salt crust that is readily dissolved during the first washing step. Accordingly, K drops below the XPS detection limit and the associated oxygen signal is strongly reduced. In contrast, for C35 the photographs indicate that potassium compounds are more embedded within the carbon structure. This interpretation is consistent with the weaker and less resolved carbonate reflections observed for unwashed C35 by XRD (Fig. S2). This lower accessibility is reflected in the XPS results, where K remains detectable after the first wash and is only removed after the second washing step. These results indicate that the effectiveness of washing is governed less by the total amount of residual potassium and more by its spatial distribution, which is directly dependent on the KOH solution volume used during impregnation of the AC precursors.

Electron microscopy of the washed ACs demonstrates that using the same precursor paper (P0) (Fig. 11a and b) but varying the KOH solution volume leads to pronounced differences in the macropore architecture (Fig. 11c–f). Since the paper fibers and the bulk paper structure can absorb only a finite volume of solution, variations in the total solution volume result in different KOH distributions within the precursor. This is reflected in the distinct spatial distribution of K-salt deposits observed in the unwashed ACs (Fig. 8c and d). Consequently, the activation proceeds via different pathways, as supported by TGA-MS data and visual inspection of the specimens after heating to 250 °C (Fig. 3b–d, f, h).

SEM analysis reveals clear differences in macroporous morphology across the AC series (Fig. 11c–f). Among all specimens, C20 exhibits the largest macropores, whereas the macropore sizes of C25, C30, and C35 are comparatively similar. In contrast, a systematic trend is observed in the pore wall thickness, which decreases progressively from C20 to C35. These morphological differences can be explained by the underlying activation mechanisms. In C35, the wet alkaline degradation stage terminates at lower temperatures than in C20, allowing a larger fraction of degraded cellulose fragments to be converted into solid carbon rather than lost as volatile species. These fragments are incorporated into the evolving carbon scaffold, promoting a higher structural density and stability. As a result, a finer macroporous structure with thinner pore walls is formed. Moreover, an additional high-temperature physical activation step at 720 °C in C20 (Fig. 2 d) contributes not only to further micropore formation but also to pore widening, producing a coarser macroporous morphology. During this process, the most exposed and fine structural features are removed, leaving a framework dominated by fewer, thicker pore walls. The intermediate specimens C25 and C30 exhibit macropore sizes similar to C35 but slightly thicker pore walls, suggesting that physical activation is present but less pronounced than in C20. C25 and C30 therefore represent an intermediate morphological regime, whereas the pronounced coarsening observed for C20 appears only when a substantially larger external KOH solution fraction is present.

High-resolution TEM of C35 (Fig. 11g and h) further reveals that, in addition to macropores, a substantial degree of microporosity is present. The micropores predominantly appear as slit-shaped voids formed between stacked graphene layers. The carbon framework of C35 appears partially ordered and turbostratic, with short, curved, and misoriented lattice fringes that locally form bent stacked lamellae. In some regions, the fringes show concentric or onion-like curvature. These features suggest the presence of small graphitic microdomains (graphene-like crystallites) rather than long-range ordered graphite, which is typical of chemically activated carbons.

Nitrogen adsorption measurements cannot probe ultra-micropores ($\leq$0.7 nm) due to the molecular size of N_2 [1]. Therefore, the obtained PSD and SSA only reflect pores accessible to N_2 and do not represent the full porosity. However, N_2 adsorption remains an important complementary technique, as it provides quantitative information on the SSA and pore volume of the micro- and mesopores that are accessible to gas molecules. The PSD (Fig. 12 a) shows that C20 exhibits the highest pore volume in the 1.2-1.3 nm range as well as in the mesopore region (2-5 nm). In contrast, C35 displays the lowest pore volume in these pore size ranges, while C25 and C30 show similar intermediate values, lying between C20 and C35. This similarity suggests that the moderate increase in solution volume from C30 to C25 does not yet create the distinctly different impregnation state observed for C20.

Considering that pore development in C20 was more strongly driven by physical activation due to the early conversion of a large fraction of KOH into potassium salts compared with specimens impregnated with lower KOH solution volume, its higher porosity in the N_2-accessible range, particularly in the mesoporous region, is reasonable. CO_2-MS data further support this interpretation, revealing CO_2 release from the interaction between K_2CO_3 and oxygen-containing groups in the char at approximately 720 °C in C20. This CO_2 evolution promotes additional pore growth, leading to increased mesopore volume and, on a larger scale, the formation of large macropores, as confirmed by SEM (Fig. 11c–f).

C20 exhibits the highest pore volume within the N_2-accessible pore size range, mainly due to its pronounced contribution of mesopores (2-5 nm), which results in the highest SSA (1455 m^2/g). The SSA decreases toward C35, reaching 1276 m^2/g. In contrast, the relative micropore contribution to the SSA (pores <2 nm) increases from 65% for C20 to 83% for C35, while remaining nearly constant for C25 and C30 (76% and 75%, respectively).

Residual potassium-containing species detected by XPS after the standard washing step may have partially reduced N_2 accessibility by occupying pore volume or constricting pore entrances. However, XPS probes only a limited near-surface region at selected positions and therefore confirms the presence of residual potassium without quantifying its distribution throughout the bulk material or internal pore network. The N_2-derived trends across the series remain clearly visible. Nevertheless, residual potassium in C30 and C35 may slightly underestimate pore volumes and SSA. This may be most relevant for micropores because salts located there are less accessible to the washing solution.

SAXS analysis (Fig. 13) indicates a decrease in the pore volume fraction from C20 to C35, which is consistent with enhanced physical activation arising from the higher K_2CO_3 presence associated with the use of larger KOH solution volumes during impregnation. This trend is in good agreement with the N_2 adsorption-derived SSA (Fig. 12 b), which likewise decreases from C20 to C35. Unlike gas adsorption, SAXS does not require pores to be accessible from the external surface and is therefore less affected by pore blockage by residual potassium salts. It thus provides complementary information on the overall nanoscale pore structure of the carbon framework. The agreement between both techniques indicates that the observed trend is not primarily caused by restricted N_2 accessibility due to residual potassium salts.

Concurrently, a shift toward smaller pore sizes is observed. The mean pore diameter decreases from 1.52 nm (C20) to 1.26 nm (C35), while all specimens remain dominated by pores in the ~1-2 nm size range, indicating that the primary microporous structure is preserved across the series. The highest observed pore volume contribution in the N_2-derived PSD occurs at approximately 0.9 nm (Fig. 12 a), whereas SAXS yields mean pore diameters of 1.26-1.52 nm. One possible explanation is that some pores contributing to the SAXS-derived mean diameter are inaccessible to N_2 because they are closed or connected through narrow bottlenecks. These pores would be absent from the N_2-derived PSD, leaving the accessible population around 0.9 nm as the highest observed contribution. However, the values are also influenced by the different measurement principles, weighting schemes, and pore-geometry assumptions of SAXS and gas adsorption and are therefore not directly comparable. CO_2 adsorption at 273 K could provide complementary

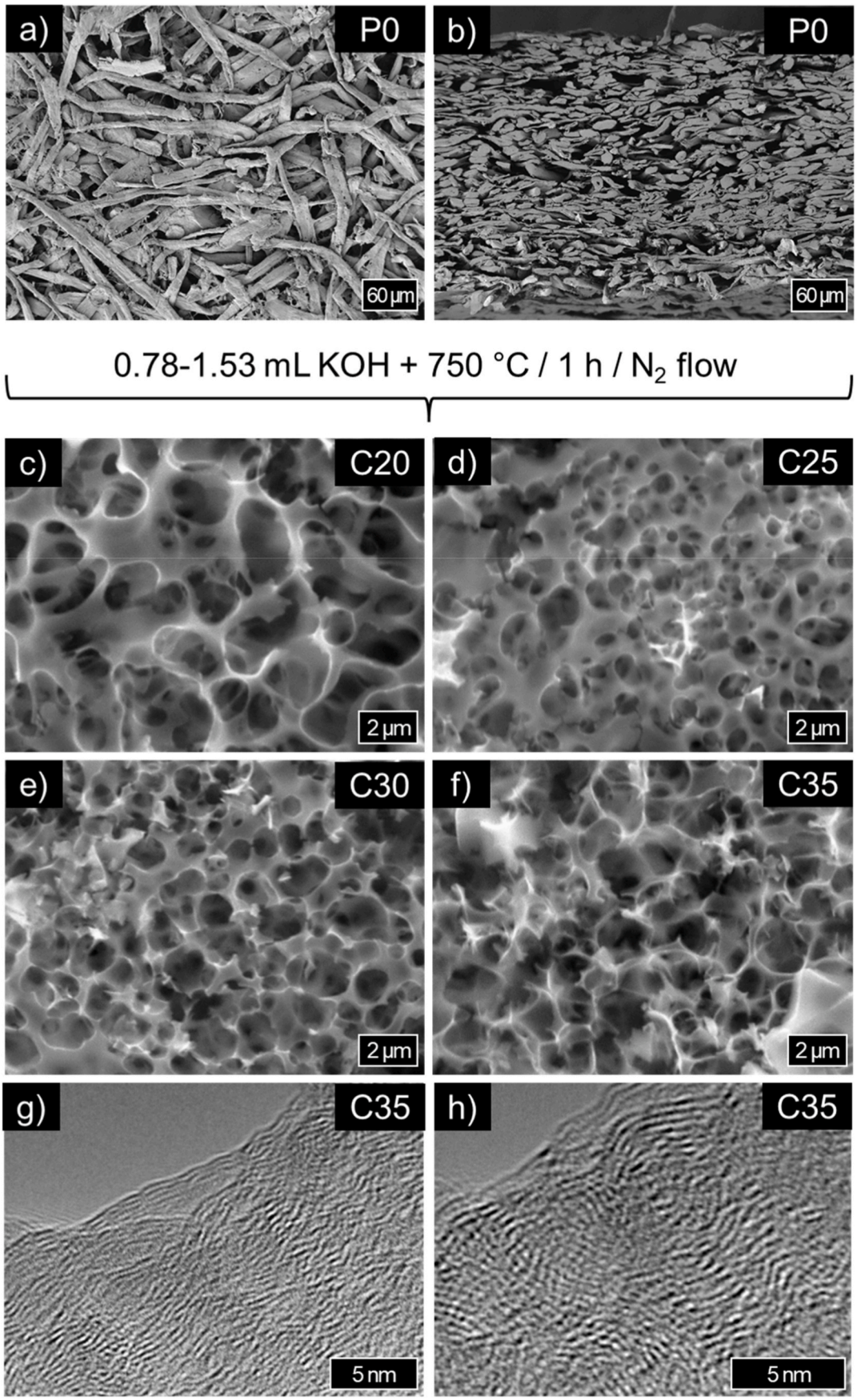

Fig. 11. Microscopy images showing SEM micrographs of the precursor paper surface (a) and cross-section (b) at 200× magnification, and of the ACs derived from it (c-f) at 3000× magnification. TEM images of the ACs produced using the lowest KOH solution volume (35 w.%) are shown in (g) and (h).

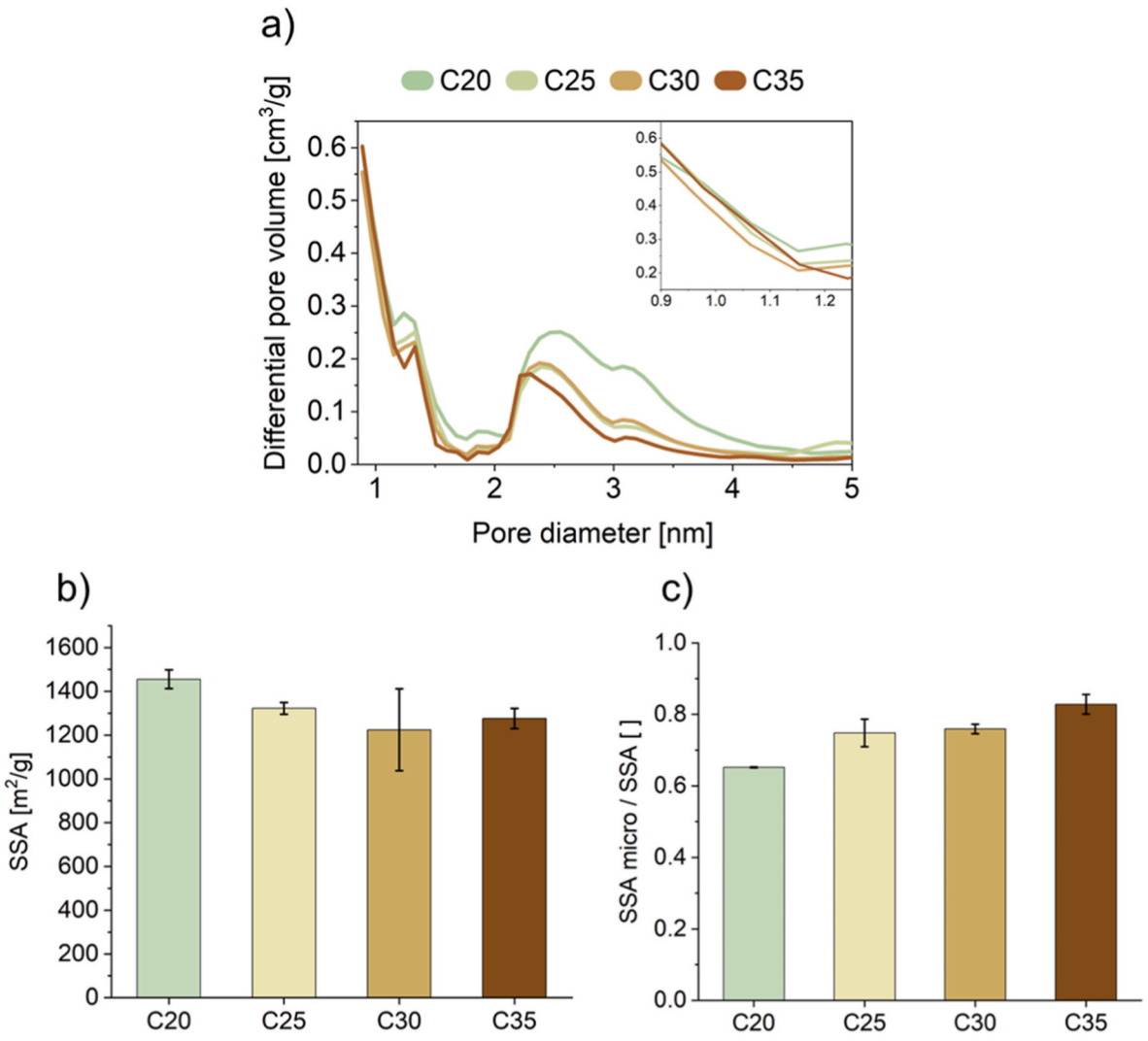

Fig. 12. Differential pore volume distributions of the ACs derived from N_2 adsorption data: (a) PSD curves, (b) total SSA and (c) micropore-SSA (pores <2 nm) calculated from N_2 adsorption measurements.

information on narrow, kinetically restricted pores and should be considered in future studies.

Beyond this modest shift in the mean pore diameter, clear differences emerge in the contribution of larger pores. In particular, C20 exhibits the highest pore volume fraction at diameters above the mean, indicating an enhanced contribution from pores in the upper micropore to small-mesopore size regime. This behavior is consistent with the most pronounced pore widening/merging, attributable to etching by CO_2 released during the reaction of K_2CO_3 and oxygen-containing groups in the char (Fig. 2 d). In contrast, the pore volume associated with these larger diameters is lower for C25 and C30, and smallest for C35.

C25 and C30 display similar PSDs in terms of both the main peak position and the overall PSD shape. Their mean pore diameters differ only slightly (1.42 nm for C30 and 1.50 nm for C25), consistent with the nearly identical N_2-derived PSDs and relative micropore contributions. This plateau may partly reflect the nonlinear increase in water addition: although the KOH concentrations differ in equal 5 w.% steps, the H_2O-to-KOH mass ratio increases by 0.67 g g^{-1} from C30 to C25 but by 1.00 g g^{-1} from C25 to C20 (Table 1). Taking 0.78 mL (C35) as the uptake limit, the external solution fraction is approximately 18% for C30, 35% for C25, and 49% for C20. Assuming that KOH is initially homogeneously distributed in the solution, similar fractions of KOH are therefore initially located outside the internal paper structure. Thus, nearly half of the KOH in C20 is already associated with the external liquid fraction before drying, compared with approximately 1/3 in C25 and less than 1/5 in C30. In addition, the larger liquid reservoir in C20 may maintain a connected aqueous phase for longer during drying. Evaporation could therefore sustain outward transport of dissolved potassium species from the sheet interior toward the evaporation front, further increasing surface enrichment through efflorescence-like redistribution (Fig. 4). In C25 and C30, the smaller liquid reservoirs are removed more rapidly, limiting the duration and extent of this redistribution. The moderate difference between C25 and C30 may therefore be insufficient to strongly change the solution-mediated transport of K-species before the salts become immobilized by drying. C20 therefore represents a different impregnation state after drying, in which the larger externally located KOH fraction may promote stronger carbonate formation, consistent with the additional high-temperature CO_2 release and pronounced pore widening.

3.8. Scope and transferability of the water volume effect

Since the observed water volume effect originates from differences in solution uptake, KOH distribution, and drying behavior, its magnitude is expected to depend on the properties of both the precursor and the activation system. More heterogeneous feedstocks may exhibit different absorption capacities, swelling behavior, and reagent accessibility, thereby shifting the solution volume at which an external liquid fraction

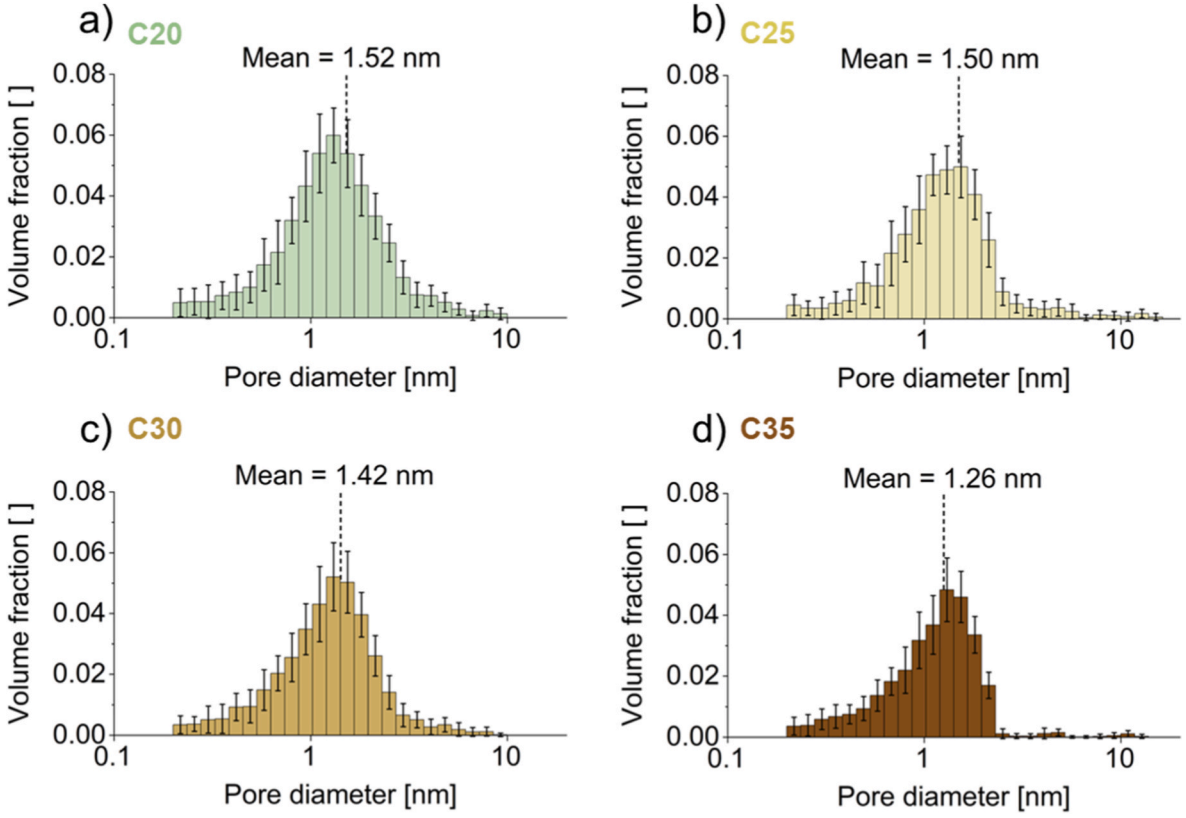

Fig. 13. PSDs of the ACs determined by SAXS: (a) C20, (b) C25, (c) C30 and (d) C35.

Table 1
Average KOH solution concentrations, corresponding volumes, and masses applied per precursor paper sheet for activation. The precursor-to-KOH mass ratio was kept constant at 1:1.

Specimens	Avg. c (KOH) [w.%]	Avg. V (KOH) [mL]	Avg. m (KOH_{dry}) [g]/ [mmol]	Avg. m (H_2O) [g]	KOH: H_2O mass ratio
C20	20	1.53	0.37/6.59	1.48	1 : 4.00
C25	25	1.20		1.11	1 : 3.00
C30	30	0.95		0.86	1 : 2.33
C35	35	0.78		0.69	1 : 1.86

* Exact values depend on the individual sheet mass, which varies by ±0.004 g.

persists. Activation temperature and KOH loading may additionally change the relative contributions of low-temperature alkaline degradation and high-temperature activation reactions. Likewise, NaOH, K_2CO_3, and mixed activator systems may show different water-volume dependencies because their solubility, hydration behavior, and reaction pathways differ from those of KOH. In dry-mixing routes, where the initial contact state is governed primarily by solid–solid contact rather than solution transport, water is also expected to play a different role. Future studies should therefore examine this relationship in less uniform feedstocks such as lignocellulosic biomass, as well as under different activation conditions and systems.

4. Conclusion

Overall, within the investigated system at an activation temperature of 750 °C and a KOH-to-precursor mass ratio of 1:1, the amount of water used to dissolve KOH acts as a decisive parameter in the one-step conversion of cellulose into AC. Changing the solution volume modifies the starting conditions for the pyrolysis, which in turn shifts the dominant activation pathway and ultimately determines carbon yield and pore structure. At high KOH solution volume (C20), the amount of solution exceeds the absorption capacity of the paper precursor. As a result, a substantial fraction of KOH remains poorly integrated with the cellulose matrix, favoring its conversion into K_2CO_3 rather than direct participation in KOH-cellulose reactions. In contrast, at lower KOH solution volume (C35), the entire solution is readily absorbed by the paper, ensuring intimate contact between KOH and cellulose throughout the precursor. Under these conditions, the external K_2CO_3 formation is less pronounced, and the relative contribution shifts toward direct chemical activation and away from CO_2-assisted activation.

In C20, the KOH present in the external solution fraction is more exposed to atmospheric and reaction-generated CO_2, promoting $KHCO_3$ and K_2CO_3 formation. The resulting carbonate-rich phase retains water and thereby prolong the hydrated alkaline environment. This delays char formation and extends the period during which cellulose undergoes alkaline degradation. Consequently, more cellulose is converted into low molecular weight volatile products that contribute less to the carbonaceous residue, thereby reducing the carbon yield. With decreasing KOH solution volume from C20 to C35, the extent of alkaline degradation is reduced, leading to earlier aromatization and char formation. Besides the apparent color change (Fig. 3), ATR-FTIR confirms that char formation already occurs at 250 °C, with the cellulose structure being largely degraded. Additionally, ATR-FTIR and XRD confirm the formation of potassium carbonate phases, assigned mainly to K_2CO_3 and $K_2CO_3{\cdot}1.5H_2O$, in samples heated to 250 °C (Fig. 7) and their persistence in the unwashed ACs after completion of the thermal program (Fig. S2).

These differences in the activation pathway also govern pore development. In C35, early charring combined with reduced volatile loss results in a dense, finely developed macroporous structure with thin pore walls. In contrast, stronger physical activation in C20 leads to the loss of fine structural features, producing a coarser morphology with thicker pore walls. The extra release of CO_2 in C20 further promotes micropore formation and micropore merging, increasing the total pore

volume and, in particular, enhancing mesoporosity. As the strength of this physical activation mechanism decreases with decreasing KOH solution volume, both the total pore volume and the mesoporous contribution generally decrease from C20 to C35. However, this trend was nonlinear, with C25 and C30 exhibiting similar microstructural properties and pronounced additional pore enlargement occurring only for C20, where the precursor uptake capacity was strongly exceeded.

Within the investigated cellulose/KOH model system, these findings demonstrate that the distribution of the activator, governed by the water volume in the applied solution, plays a central role in the thermal transformation of cellulose. Beyond the KOH loading and thermal conditions conventionally used to tune porosity, the extent to which a fixed KOH mass is absorbed into the bulk of the precursor versus remaining externally located governs reaction pathways, pore evolution, and carbon yield. Consequently, a carefully designed impregnation strategy provides a practical means of tuning AC pore structure toward the requirements of different applications and represents a key parameter for the scale-up of one-step KOH activation processes. Because paper provides a reproducible cellulose network with a defined liquid-uptake capacity, the quantitative relationship observed here may shift for more heterogeneous biomass feedstocks with different compositions, structures, and absorption behavior. Its transferability to such feedstocks, as well as to other activation conditions and systems, therefore remains to be established.

CRediT authorship contribution statement

Alexa Scheer: Conceptualization, Methodology, Writing – original draft. **Hoang Bao Tran Nguyen:** Conceptualization, Methodology, Writing – review & editing. **Johanna Fischer:** Conceptualization, Writing – review & editing. **Glen J. Smales:** Methodology, Writing – review & editing. **Julian Selinger:** Methodology, Writing – review & editing. **Ahmad Alem:** Methodology, Writing – review & editing. **Christine Bandl:** Methodology, Writing – review & editing. **Steffen Fischer:** Conceptualization, Funding acquisition, Writing – review & editing. **Daria Mikhailova:** Conceptualization, Funding acquisition, Writing – review & editing. **Stefan Spirk:** Conceptualization, Funding acquisition, Supervision, Writing – review & editing.

Declaration of competing interest

The authors declare the following financial interests/personal relationships which may be considered as potential competing interests:1. Stefan Spirk reports financial support was provided by Austrian Science Fund. He also reports to be cofounder and CEO of Ecolyte GmbH. The other authors, declare that they have no known competing financial interests or personal relationships that could have appeared to influence the work reported in this paper.

Acknowledgements

This research was funded by the Austrian Science Fund (FWF) [10.55776/I6403] and the German Research Foundation (DFG), project number 511521214 (FI755/16-1, MI945/8-1). . For open access purposes, the author has applied a CC BY public copyright license to any author-accepted manuscript version arising from this submission. The authors acknowledge Aalto University for providing facilities and technical support at the OtaNano Nanomicroscopy Center (Aalto-NMC). The authors would like to acknowledge the support of the Somapp Lab, a core facility supported by the Austrian Federal Ministry of Education, Science and Research, the Graz University of Technology and Anton Paar GmbH.The authors also thank Roberto J. Aguado for his helpful comments and suggestions that improved the manuscript, and Klaus Reichmann for providing access to facilities for thermal analysis.

During the preparation of this work the authors used ChatGPT-5.2 in order to identify suitable synonyms, phrases, and linking text to improve clarity and coherence. After using this tool/service, the authors reviewed and edited the content as needed and take full responsibility for the content of the published article.

Appendix A. Supplementary data

Supplementary data to this article can be found online at https://doi.org/10.1016/j.carbon.2026.121941.

References

[1] A. Scheer, G.J. Smales, H.B.T. Nguyen, J. Rattenberger, C. Mayrhofer, J. Fischer, S. Fischer, D. Mikhailova, S. Spirk, Influence of precursor structure on KOH-activated carbon: a study using tunable all-cellulose composites, Carbon 247 (2026) 121036, https://doi.org/10.1016/j.carbon.2025.121036.
[2] S. Stock, N. Kostoglou, J. Selinger, S. Spirk, C. Tampaxis, G. Charalambopoulou, T. Steriotis, C. Rebholz, C. Mitterer, O. Paris, Coffee waste-derived nanoporous carbons for hydrogen storage, ACS Appl. Energy Mater. 5 (9) (2022) 10915–10926, https://doi.org/10.1021/acsaem.2c01573.
[3] Z. Zhang, T. Wang, H. Zhang, Y. Liu, B. Xing, Adsorption of Pb(II) and Cd(II) by magnetic activated carbon and its mechanism, Sci. Total Environ. 757 (2021) 143910, https://doi.org/10.1016/j.scitotenv.2020.143910.
[4] J. Selinger, K. Meinander, B.P. Wilson, Q. Abbas, M. Hummel, S. Spirk, Sweet side streams: sugar beet pulp as source for high-performance supercapacitor electrodes, ACS Omega 9 (4) (2024) 4733–4743, https://doi.org/10.1021/acsomega.3c07976.
[5] J. Fischer, L. Wolfram, S. Oswald, S. Fischer, D. Mikhailova, Carbons derived from regenerated spherical cellulose as anodes for Li-Ion batteries at elevated temperatures, ChemPhysChem 25 (8) (2024) e202300833, https://doi.org/10.1002/cphc.202300833.
[6] J. Serafin, B. Dziejarski, C. Solis, P. Ramírez de la Piscina, N. Homs, Medium-pressure hydrogen storage on activated carbon derived from biomass conversion, Fuel 363 (2024) 130975, https://doi.org/10.1016/j.fuel.2024.130975.
[7] B. Dziejarski, J. Serafin, D.F. Hernández-Barreto, E. Naumovska, J. Sreńscek-Nazzal, N. Klomkliang, E. Tam, R. Krzyżyńska, K. Andersson, P. Knutsson, Tailoring highly surface and microporous activated carbons (ACs) from biomass via KOH, $K_2C_2O_4$ and KOH/K2C2O4 activation for efficient CO_2 capture and CO2/N2 selectivity: characterization, experimental and molecular simulation insights, Chem. Eng. J. 524 (2025) 169677, https://doi.org/10.1016/j.cej.2025.169677.
[8] W. Qin, Y. Dong, H. Jiang, W.H. Loh, J. Imbrogno, T.M. Swenson, O. Garcia-Rodriguez, O. Lefebvre, A new approach of simultaneous adsorption and regeneration of activated carbon to address the bottlenecks of pharmaceutical wastewater treatment, Water Res. 252 (2024) 121180, https://doi.org/10.1016/j.watres.2024.121180.
[9] Y. Zhao, E.E. Taylor, X. Hu, B. Evanko, X. Zeng, H. Wang, R. Ohnishi, T. Tsukazaki, J.-F. Li, N.P. Stadie, S.J. Yoo, G.D. Stucky, S.W. Boettcher, What structural features make porous carbons work for redox-enhanced electrochemical capacitors? A fundamental investigation, ACS Energy Lett. 6 (3) (2021) 854–861, https://doi.org/10.1021/acsenergylett.0c02424.
[10] R.J. Bragg, K. Griffiths, I. Hwang, M. Leketas, K. Polus, V. Presser, R.A.W. Dryfe, J. M. Griffin, Solvation effects on aqueous ion adsorption and electrosorption in carbon micropores, Carbon 229 (2024) 119531, https://doi.org/10.1016/j.carbon.2024.119531.
[11] J. Serafin, B. Dziejarski, O.F. Cruz Junior, J. Sreńscek-Nazzal, Design of highly microporous activated carbons based on walnut shell biomass for H2 and CO2 storage, Carbon 201 (2023) 633–647, https://doi.org/10.1016/j.carbon.2022.09.013.
[12] G. Conte, A. Policicchio, M. Idrees, G. Desiderio, R.G. Agostino, Tuning the ultra-microporosity in hierarchical porous carbons derived from amorphous cellulose towards a sustainable solution for hydrogen storage, Int. J. Hydrogen Energy 50 (2024) 763–773, https://doi.org/10.1016/j.ijhydene.2023.08.128.
[13] D.A. Khuong, H.N. Nguyen, T. Tsubota, Activated carbon produced from bamboo and solid residue by CO2 activation utilized as CO2 adsorbents, Biomass Bioenergy 148 (2021) 106039, https://doi.org/10.1016/j.biombioe.2021.106039.
[14] Y. Zhang, Y.-P. Zhao, L.-L. Qiu, J. Xiao, F.-P. Wu, J.-P. Cao, Y.-H. Bai, F.-J. Liu, Insights into the KOH activation parameters in the preparation of corncob-based microporous carbon for high-performance supercapacitors, Diam. Relat. Mater. 129 (2022) 109331, https://doi.org/10.1016/j.diamond.2022.109331.
[15] Y. Li, J. Mei, L. Wu, Q. Xu, Z. Li, Ultrahigh surface area hierarchical porous carbon derived from biomass via a new KOH activation strategy for high-performance supercapacitor, Int. J. Hydrogen Energy 49 (2024) 67–80, https://doi.org/10.1016/j.ijhydene.2023.10.319.
[16] J.M. Illingworth, B. Rand, P.T. Williams, Understanding the mechanism of two-step, pyrolysis-alkali chemical activation of fibrous biomass for the production of activated carbon fibre matting, Fuel Process. Technol. 235 (2022) 107348, https://doi.org/10.1016/j.fuproc.2022.107348.
[17] M. Wei, F. Marrakchi, C. Yuan, X. Cheng, D. Jiang, F.F. Zafar, Y. Fu, S. Wang, Adsorption modeling, thermodynamics, and DFT simulation of tetracycline onto mesoporous and high-surface-area NaOH-activated macroalgae carbon, J. Hazard Mater. 425 (2022) 127887, https://doi.org/10.1016/j.jhazmat.2021.127887.
[18] H. Niu, H. Jin, Q. Sun, Y. Shi, X. Zhang, Y. Cai, Activation of biochars by waste phosphoric acids: an integrated disposal route of waste acids and solid waste, ACS Sustain. Chem. Eng. 9 (48) (2021) 16403–16414, https://doi.org/10.1021/acssuschemeng.1c06326.

[19] A. Alcazar-Ruiz, S. Maisano, V. Chiodo, F. Urbani, F. Dorado, L. Sanchez-Silva, Enhancing CO2 capture performance through activation of olive pomace biochar: a comparative study of physical and chemical methods, Sustain. Mater. Technol. 42 (2024) e01177, https://doi.org/10.1016/j.susmat.2024.e01177.
[20] W. Chen, M. Gong, K. Li, M. Xia, Z. Chen, H. Xiao, Y. Fang, Y. Chen, H. Yang, H. Chen, Insight into KOH activation mechanism during biomass pyrolysis: chemical reactions between O-containing groups and KOH, Appl. Energy 278 (2020) 115730, https://doi.org/10.1016/j.apenergy.2020.115730.
[21] T. Fischer, A. Kretzschmar, V. Selmert, S. Jovanovic, H. Kungl, H. Tempel, R. A. Eichel, Post-treatment strategies for pyrophoric KOH-activated carbon nanofibres, RSC Adv. 14 (6) (2024) 3845–3856, https://doi.org/10.1039/D3RA07096D.
[22] P. Ozpinar, C. Dogan, H. Demiral, U. Morali, S. Erol, C. Samdan, D. Yildiz, I. Demiral, Activated carbons prepared from hazelnut shell waste by phosphoric acid activation for supercapacitor electrode applications and comprehensive electrochemical analysis, Renew. Energy 189 (2022) 535–548, https://doi.org/10.1016/j.renene.2022.02.126.
[23] S.D. Magar, C. Leibing, J.L. Gómez-Urbano, D. Carriazo, A. Balducci, Brewers' spent grains-derived carbon as anode for alkali metal-ion batteries, Energy Technol. 10 (9) (2022) 2200379, https://doi.org/10.1002/ente.202200379.
[24] S. Tabac-Agam, S. Burda, S.M. Zahan, D.R. Dekel, D. Eisenberg, Biomass or biomess: tackling reproducibility in biomass-derived carbon electrocatalysts, Catal. Sci. Technol. 15 (19) (2025) 5678–5689, https://doi.org/10.1039/D4CY00991F.
[25] H. Xia, W. Kong, L. Liu, K. Lin, H. Li, Effects of harvest time and desalination of feedstock on Spartina alterniflora biochar and its efficiency for Cd2+ removal from aqueous solution, Ecotoxicol. Environ. Saf. 207 (2021) 111309, https://doi.org/10.1016/j.ecoenv.2020.111309.
[26] J.B. Schaubeder, C. Guizani, J. Selinger, A. Mautner, M. Hummel, S. Spirk, Design of experiments as a tool to guide the preparation of tailor-made activated carbons, Sci. Rep. 13 (1) (2023) 3977, https://doi.org/10.1038/s41598-023-30642-8.
[27] C. Guizani, O. Sorsa, V. Siipola, T. Ohra-Aho, R. Paalijärvi, A. Pasanen, M. Mäkelä, A. Kalliola, M. Vilkman, K. Torvinen, The effects of lignin structure on the multiscale properties and electrochemical performance of activated carbons, Biomass Convers. Biorefinery 14 (17) (2024) 21149–21163, https://doi.org/10.1007/s13399-023-04373-9.
[28] Y. Li, Z. Sun, L. Zhang, Y. Zou, N. Yao, W. Lei, T. Jiang, Y. Chen, G.Z. Chen, High yield and packing density activated carbon by one-step molecular level activation of hydrophilic pomelo peel for supercapacitors, J. Electrochem. Soc. 168 (6) (2021) 060521, https://doi.org/10.1149/1945-7111/ac0762.
[29] J. Peng, Y. Huang, R. Fu, J. Lu, W. Wang, W. Zhu, Y. Yu, F. Guo, H. Mai, Microscopic dissolution process of cellulose in alkaline aqueous solvents and its application in CNFs extraction - investigating temperature as a variable, Carbohydr. Polym. 322 (2023) 121361, https://doi.org/10.1016/j.carbpol.2023.121361.
[30] D.A. Khuong, T. Tsubota, H.N. Nguyen, Comprehensive understanding of the impact of alkaline-activated bamboo-derived carbon for enhancing supercapacitor performance, J. Phys. Chem. C 128 (41) (2024) 17313–17327, https://doi.org/10.1021/acs.jpcc.4c04228.
[31] P. Liu, S. Sun, S. Huang, Y. Wu, X. Li, X. Wei, S. Wu, KOH activation mechanism in the preparation of brewer's spent grain-based activated carbons, Catalysts 14 (11) (2024) 814, https://doi.org/10.3390/catal14110814.
[32] J.Y. Son, S. Choe, Y.J. Jang, H. Kim, Waste paper-derived porous carbon via microwave-assisted activation for energy storage and water purification, Chemosphere 355 (2024) 141798, https://doi.org/10.1016/j.chemosphere.2024.141798.
[33] R. He, M. Neupane, A. Zia, X. Huang, C. Bowers, M. Wang, J. Lu, Y. Yang, P. Dong, Binder-free wood converted carbon for enhanced water desalination performance, Adv. Funct. Mater. 32 (49) (2022) 2208040, https://doi.org/10.1002/adfm.202208040.
[34] V. Gómez-Serrano, E.M. Cuerda-Correa, M.C. Fernández-González, M.F. Alexandre-Franco, A. Macías-García, Preparation of activated carbons from chestnut wood by phosphoric acid-chemical activation. Study of microporosity and fractal dimension, Mater. Lett. 59 (7) (2005) 846–853, https://doi.org/10.1016/j.matlet.2004.10.064.
[35] J. Phiri, H. Ahadian, M. Sandberg, K. Granström, T. Maloney, The influence of physical mixing and impregnation on the physicochemical properties of pine wood activated carbon produced by one-step ZnCl2 activation, Micromachines 14 (3) (2023) 572, https://doi.org/10.3390/mi14030572.
[36] Y. Shi, J. Wang, Y. Li, Z. Sui, X. Xu, Unveiling the ambient CO2-mediated K2CO3 activation pathway in KOH post-treated activated carbon for exceptional SF6 adsorption, Chem. Eng. J. 520 (2025) 166100, https://doi.org/10.1016/j.cej.2025.166100.
[37] H. Chen, Z. Tang, B. Liu, W. Chen, J. Hu, Y. Chen, H. Yang, The new insight about mechanism of the influence of K2CO3 on cellulose pyrolysis, Fuel 295 (2021) 120617, https://doi.org/10.1016/j.fuel.2021.120617.
[38] D. Zhao, H. Feng, Y. Wang, F. Wang, H. Wang, H. Liu, H. Liu, Influence mechanism of K on cellulose pyrolysis by stepwise isothermal method in-situ DRIFTS method, Fuel 360 (2024) 130601, https://doi.org/10.1016/j.fuel.2023.130601.
[39] M. Hu, Z. Ye, Q. Zhang, Q. Xue, Z. Li, J. Wang, Z. Pan, Towards understanding the chemical reactions between KOH and oxygen-containing groups during KOH-catalyzed pyrolysis of biomass, Energy 245 (2022) 123286, https://doi.org/10.1016/j.energy.2022.123286.
[40] B.R. Pauw, A. Smith, T. Snow, N. Terrill, A. Thünemann, The modular small-angle X-ray scattering data correction sequence, J. Appl. Crystallogr. 50 (6) (2017) 1800–1811, https://doi.org/10.1107/S1600576717015096.
[41] J. Filik, A.W. Ashton, P.C.Y. Chang, P. Chater, S. Day, M. Drakopoulos, M. Gerring, M. Hart, O. Magdysyuk, S. Michalik, Processing two-dimensional X-ray diffraction and small-angle scattering data in DAWN 2, J. Appl. Crystallogr. 50 (3) (2017) 959–966, https://doi.org/10.1107/S1600576717004708.
[42] B.R. Pauw, I. Breßler, McSAS3: improved Monte Carlo small-angle scattering analysis software for dilute and dense scatterers, arXiv preprint arXiv:2601.18659 (2026), https://doi.org/10.48550/arXiv.2601.18659.
[43] I.D. Sills, S. He, Determination of evolved gas transfer time from a thermoanalyser to a coupled gas detection system using pyrite oxidation, Thermochim. Acta 339 (1) (1999) 125–130, https://doi.org/10.1016/S0040-6031(99)00292-0.
[44] L. Fliri, K. Dubivka, D. Rusakov, A. Volikov, C. Guizani, S. Hietala, S. Filonenko, M. Hummel, Identification of a polyfuran network as the initial carbonization intermediate in cellulose pyrolysis: a comparative analysis with cellulosic hydrochars, J. Anal. Appl. Pyrolysis 181 (2024) 106591, https://doi.org/10.1016/j.jaap.2024.106591.
[45] A. Parihar, J. Vongsvivut, S. Bhattacharya, Synchrotron-based infra-red spectroscopic insights on thermo-catalytic conversion of cellulosic feedstock to levoglucosenone and furans, ACS Omega 4 (5) (2019) 8747–8757, https://doi.org/10.1021/acsomega.8b03681.
[46] P. Gao, G. Li, F. Yang, X.-N. Lv, H. Fan, L. Meng, X.-Q. Yu, Preparation of lactic acid, formic acid and acetic acid from cotton cellulose by the alkaline pre-treatment and hydrothermal degradation, Ind. Crop. Prod. 48 (2013) 61–67, https://doi.org/10.1016/j.indcrop.2013.04.002.
[47] G. Liu, H. Lu, K. Wu, G. Guan, B. Liang, Co-production of high-purity hydrogen and value-added molecules from cellulose under alkaline environment: mechanism and application, Renew. Energy 252 (2025) 123472, https://doi.org/10.1016/j.renene.2025.123472.
[48] G. Wang, Y. Meng, J. Zhou, L. Zhang, Selective hydrothermal degradation of cellulose to formic acid in alkaline solutions, Cellulose 25 (10) (2018) 5659–5668, https://doi.org/10.1007/s10570-018-1979-9.
[49] M. Gunnarsson, D. Bernin, M. Hasani, M. Lund, E. Bialik, Direct evidence for reaction between cellulose and CO2 from nuclear magnetic resonance, ACS Sustain. Chem. Eng. 9 (42) (2021) 14006–14011, https://doi.org/10.1021/acssuschemeng.1c05863.
[50] K. Gluch, J. Cytawa, L. Michalak, Electron impact ionization of acetaldehyde, Int. J. Mass Spectrom. 273 (1–2) (2008) 20–23, https://doi.org/10.1016/j.ijms.2008.02.006.
[51] K. Lansdown, C.M. Heppell, M. Dossena, S. Ullah, A.L. Heathwaite, A. Binley, H. Zhang, M. Trimmer, Fine-scale in situ measurement of riverbed nitrate production and consumption in an armored permeable riverbed, Environ. Sci. Technol. 48 (8) (2014) 4425–4434, https://doi.org/10.1021/es4056005.
[52] X. Wang, X. Feng, Y. Ma, Activated carbon from chili straw: K2CO3 activation mechanism, adsorption of dyes, and thermal regeneration, Biomass Convers. Biorefinery 14 (16) (2024) 19563–19580, https://doi.org/10.1007/s13399-023-04173-1.
[53] M. Baldassarre, A. Barth, The carbonate/bicarbonate system as a pH indicator for infrared spectroscopy, Analyst 139 (9) (2014) 2167–2176.
[54] J.L. Bishop, S.J. King, M.D. Lane, A.J. Brown, B. Lafuente, T. Hiroi, R. Roberts, G. A. Swayze, J.F. Lin, M. Sánchez Román, Spectral properties of anhydrous carbonates and nitrates, Earth Space Sci. 8 (10) (2021), https://doi.org/10.1029/2021EA001844 e2021EA001844.
[55] Y. Kim, M.-C. Caumon, O. Barres, A. Sall, J. Cauzid, Identification and composition of carbonate minerals of the calcite structure by Raman and infrared spectroscopies using portable devices, Spectrochim. Acta Mol. Biomol. Spectrosc. 261 (2021) 119980, https://doi.org/10.1016/j.saa.2021.119980.
[56] A. Ameri, Density, refractive index, electrical conductivity, pH, and FT-IR and UV–Vis spectra of potassium carbonate–potassium bicarbonate–water system, J. Chem. Eng. Data 70 (2) (2025) 766–786, https://doi.org/10.1021/acs.jced.4c00489.
[57] D.E. Nixon, G.S. Parry, A.R.J.P. Ubbelohde, Order-disorder transformations in graphite nitrates, Proceedings of the Royal Society of London. A. Mathematical and Physical Sciences 291 (1426) (1966) 324–339, https://doi.org/10.1098/rspa.1966.0098.
[58] J.M.S. Skakle, M. Wilson, J. Feldmann, Dipotassium carbonate sesquihydrate: rerefinement against new intensity data, Acta Crystallogr. E 57 (11) (2001) i94–i97, https://doi.org/10.1107/S1600536801016312.
[59] Y. Idemoto, J.W. Richardson, N. Koura, S. Kohara, C.-K. Loong, Crystal structure of (LixK1 −x)2CO3 (x = 0, 0.43, 0.5, 0.62, 1) by neutron powder diffraction analysis, J. Phys. Chem. Solid. 59 (3) (1998) 363–376, https://doi.org/10.1016/S0022-3697(97)00209-6.
[60] T.M. Gesing, L. Robben, Determination of the average crystallite size and the crystallite size distribution: the envelope function approach EnvACS, J. Appl. Crystallogr. 57 (5) (2024) 1466–1476, https://doi.org/10.1107/S1600576724007362.